Unmixing of magnetic hysteresis loops through a modified Gamma-Cauchy exponential model

U. D. Bellon[1,2], R. I. F. Trindade[1], and W. Williams[2]

[1] Department of Geophysics, Institute of Astronomy, Geophysics and Atmospheric Sciences of the University of São Paulo (IAG-USP). Rua do Matão, São Paulo, Brazil.

[2] School of Geosciences, University of Edinburgh, United Kingdom.

Corresponding authors: Ualisson Bellon (ualisson.bellon@usp.br), Wyn Williams (wyn.williams@ed.ac.uk)

Key Points:

- A new method for the parametric unmixing of magnetic hysteresis data based on modified Gamma-Cauchy exponential model is presented
- The model accounts for curves with variable skewness/kurtosis, allowing the separation of dia/para and ferromagnetic contributions
- An open-sourced Python script (*Hist-unmix)* allows the users to import, process and model their data on a friendly interface.

Abstract

Quantifying the contributions of distinct mineral populations in bulk magnetic experiments greatly enhances the analysis of environmental and rock magnetism studies. Here we develop a new method of parametric unmixing of susceptibility components in hysteresis loops. Our approach is based on a modified Gamma-Cauchy exponential model, that accounts for variable skewness and kurtosis. The robustness of the model is tested with synthetic curves that examine the effects of noise, sampling, and proximity of susceptibility components. We provide a Python-based script, the *Hist-unmix* package, which allows the user to adjust a direct model of up to three ferromagnetic components as well as a dia/paramagnetic contribution. Optimization of all the parameters is achieved through least squares fit (Levenberg-Marquardt method), with uncertainties of each inverted parameter calculated through a Monte Carlo error propagation approach. For each ferromagnetic component, it is possible to estimate the magnetization saturation (M_s), magnetization saturation of remanence (M_{rs}) and the mean coercivity (B_c). Finally, *Hist-unmix* was applied to a set of weakly magnetic carbonate rocks from Brazil, which typically show distorted hysteresis cycles (wasp-waisted and potbellied loops). For these samples, we resolved two components with distinct coercivities. These results are corroborated by previous experimental data, showing that the lower branch of magnetic hysteresis can be modeled by the presented approach and might offer important mineralogical information for rock magnetic and paleomagnetic studies.

Keywords: Unmixing magnetic hysteresis, Python package, Magnetic mineralogy, Palaeomagnetism, Rock and mineral magnetism, Inverse theory

Plain Language Summary

Rocks contain magnetic minerals that record Earth's varying magnetic field shape and intensity, and provide information about our planets evolution, as well as the ancient environmental conditions where the rocks formed. To study these magnetic minerals, we need to identify and quantify them, but this is challenging because of the complex mixture of such minerals that a rock may contain. Magnetic hysteresis curves are a simple and quick measurement that provides information on the magnetic properties of a rock, reflecting the combined effects of different minerals. In this paper, we propose a mathematical model that can separate the individual contributions of each magnetic population. We also provide an open-source python application for users to apply our model to their own data.

1 Introduction

Magnetic minerals are used in many fields of science as important indicators of physical, chemical and biological processes (Butler, 1992; J. Dunlop & Özdemir, 1997; Liu et al., 2012; Tauxe, 2005). Typically, magnetic measurements are time and cost-effective, and can detect magnetic particles even at trace levels. Usually, natural samples will contain a mixture of magnetic mineral populations, such as oxides (e.g, magnetite and hematite), hydroxides (e.g., goethite and limonite) and iron sulphides (e.g., pyrrhotite and greigite), each with different ranges of grain-sizes. Distinguishing between these populations is not a simple task, since these properties are nonlinear functions of grain size and composition (Robertson & France, 1994). The investigation of magnetic properties in natural samples often requires the combination of many techniques, including thermomagnetic observations, such as variations of magnetic

susceptibility or magnetic induction with temperature, thermal demagnetization, magnetic hysteresis, first order reversal curves (FORCs), and alternating field demagnetization (AF), or the acquisition of artificial remanences, such as the anhysteretic remanent magnetization (ARM) and the isothermal remanent magnetization (IRM). Magnetic hysteresis and IRM acquisition measurements are quickly achieved using modern vibrating sample magnetometers (VSM), and their advantage lies on their ability to examine a wide range of coercivities, offering a quick response to the bulk magnetic properties of a rock or sediment even with small amounts of sample. For magnetic hysteresis, the shape of some curves typically suggests the presence of more than one magnetic component. These include: wasp-waisted (constricted middles, near the origin of the coercivity axis), potbellies (spreading middles near the origin and slouching shoulders) and goose-necked (constricted middles and spreading shoulders) (Tauxe et al., 1996). In some cases, these hysteresis shapes have been considered as a fingerprint of some geological processes, such as remagnetization of carbonate rocks (Jackson & Swanson-Hysell, 2012). This evaluation, however, is usually done qualitatively, without quantitative identification and separation of magnetic components.

To deal with magnetic hysteresis data, there are free-access interfaces that allow advanced processing of data like *HystLab* of Paterson et al. (2018), but unmixing of distorted curves is not a focus on their work. There are several ways to unmixing magnetic mineral populations from magnetic hysteresis, Some authors model the magnetic properties of natural materials by assuming end members in a mixture, which could be either pure magnetic phases with different grain sizes, or typical mineral sources in the study area or region, or yet end members identified from the data itself (Jackson & Solheid, 2010; Thompson, 1986). Another approach requires the fitting of basis functions to the hysteresis loops. In this case, the linear combination of different basis functions representing the different magnetic populations should represent the bulk behavior of the magnetic assemblage (Heslop, 2015). The advantage of this approach is that it requires little to no a priori information, relying on the ability of a mathematical model to represent a physical phenomenon (von Dobeneck, 1996; Vasquez & Fazzito, 2020).

Recently, a simple solution for the unmixing of magnetic components by fitting Lorentzian curves to the lower branch of magnetic hysteresis loops was proposed (Vasquez & Fazzito, 2020). It considers the magnetization (M) acquired through the induction of an applied field (B) as expressed by:

$$M(x) = (\kappa_0 \cdot B) + \frac{A}{\pi} \cdot arctan\left(\frac{2 \cdot (B - B_c)}{\theta}\right)$$

Eq. 1

The first term of the *Eq. 1* describes a linear magnetization acquired through an inducing field B, which is the dia/paramagnetic contribution to $M(B)$. Consequently, the second (and non-linear) term represents the ferromagnetic contribution, while A is the total area under the $M(x)$ curve. If B_c is equal to B, the ferromagnetic contribution will be zero, which is the very definition of coercive force. If B approaches the infinity, *Eq. 1* will tend to $A/2$, which is the magnetization saturation (M_s) of $M(B)$. Now, if *Eq. 1* is evaluated at zero field ($B = 0$), then saturation remanence (M_{rs}) is also easily calculated. The magnetic susceptibility (κ) is sequentially computed as:

$$\kappa(B) = \frac{\partial}{\partial B} M(B) = \kappa_0 + \left(\frac{2 \cdot A}{\pi}\right) \cdot \left[\frac{\theta}{(4 \cdot (B - B_c)^2) + \theta^2}\right] \quad \textit{Eq. 2}$$

In order to model the susceptibility components, one of the branches of a magnetic hysteresis (covering both the reversible and irreversible segments) is used to calculate a numerical derivative. Vasquez and Fazzito (2020) fitted the parameters of *Eq. 2* using a generic inversion routine through commercial and/or free-software and report coherent results in the unmixing of components from previously published data (Roberts et al., 1995) and from their own synthetic samples, but acknowledge that the simplicity of the model might fail to cover more complex scenarios. Such a case could arise from the contribution of fine SD-like particles (e.g., a Stoner-Wohlfarth assemblage - Stoner and Wohlfarth, 1991). A distribution of such grains might cause the reversible and irreversible segments of a lower branched magnetic hysteresis to be very different, which will originate an asymmetry. Furthermore, for viscous SD-like particles, the irreversible segment may abruptly start at $B = 0$, leading to a discontinuous derivative (Egli, 2021). Neither of these cases can be explained by a symmetrical Lorentzian curve of the form of *Eq. 2*, and would require a skewness' control parameter, similar to the coercivity analysis of Egli (2003). Finally, it is also important to consider that *Eq. 2* does not account for the approach-to-saturation behavior expected in high-fields (Fabian, 2006) and so an additional parameter is required to account for a variable kurtosis and susceptibility components with different tails.

To achieve a more robust phenomenological model to unmix susceptibility components from magnetic hysteresis data, we introduce the use of generalized gamma-Cauchy exponential distributions (Alzaatreh et al., 2016). We present a Python-based (*ipynb-file*) open-source application (*Hist-unmix*) that can be used to perform unmixing of hysteresis curves (Bellon et al., 2023). A forward model of up to three susceptibility components is demonstrated, as well as the mathematical formulation to optimize initial parameters in our inverse model, with uncertainty estimates of the parameters determined through a Monte-Carlo error propagation. We also perform numerical tests on synthetic data to assess the sensibility of a modified Gamma-Cauchy Exponential fit (*mGC*), evaluating the effect of (i) sampling, (ii) signal/noise ratio, (iii) similarity of components and the (iv) ambiguity of the model. Finally, we test the *Hist-unmix* application on distorted hysteresis loops of Neoproterozoic remagnetized rocks from São Francisco craton (Brazil), comparing the information recovered from the *Hist-unmix* package with previous rock-magnetism/paleomagnetic data

2 Materials and Methods

2.1 Forward model

Cauchy distributions have many applications in mechanical and electrical theory, often referred to as Lorentzian distributions in the physics literature. To achieve a forward model for the first derivative of a lower branched magnetic hysteresis, we propose the use of the probability density function of a gamma-Cauchy exponential distribution (*GC*(*α, β, θ*)). In such, if a random variable follows a gamma distribution with parameters *α* and *β*, a *GC*(*α, β, θ*)'s probability density function is defined as (Alzaatreh et al., 2016):

$$f(B) = \frac{\left[-log\left(0.5 - \pi^{-1} \cdot arctan\left(\frac{B}{\theta}\right)\right)\right]^{\alpha-1} \cdot \left[0.5 - \pi^{-1} \cdot arctan\left(\frac{B}{\theta}\right)\right]^{\frac{1}{\beta}-1}}{\pi \cdot \theta \cdot \beta^{\alpha} \cdot \Gamma(\alpha) \cdot \left[1 + \left(\frac{B}{\theta}\right)^{2}\right]}, x \in \mathbb{R} \quad (3)$$

Eq. 3

In Eq. 3, θ has the role of a dispersion parameter (such as in the symmetrical Lorentzian functions) and $\Gamma(\alpha)$ is the gamma function of α. The advantage of using functions of the from *GC*(α, β, θ) lies in the fact that their morphology can be symmetrical, right or left skewed, and cover a wide range of kurtosis (Alzaatreh et al., 2016). Since *Eq. 3* will peak in the arithmetic mean of B, we added a term to represent the coercivity (B_c) in a gamma-Cauchy distribution. To improve convergence, a scale factor (I) is further included, which represents the contribution ratio of each ferromagnetic component. Our modified gamma-Cauchy exponential function, $mGC(B_c, \alpha, \beta, \theta, I)$ for magnetic susceptibility becomes:

$$\kappa = \left[\frac{\left[-log\left(0.5 - \pi^{-1} \cdot arctan\left(\frac{B - B_c}{\theta}\right)\right)\right]^{\alpha-1} \cdot \left[0.5 - \pi^{-1} \cdot arctan\left(\frac{B - B_c}{\theta}\right)\right]^{\frac{1}{\beta}-1}}{\pi \cdot \theta \cdot \beta^{\alpha} \cdot \Gamma(\alpha) \cdot \left[1 + \left(\frac{B - B_c}{\theta}\right)^{2}\right]}\right] \cdot I \quad (4)$$

Eq. 4

Eq. 4 accounts for the ferromagnetic contribution to the susceptibility κ. We call this a ferromagnetic susceptibility component (*C*). A para/diamagnetic contribution (κ_0) to the magnetic susceptibility given by N-ferromagnetic components (C_N) can be calculated, for a 1D-array containing the applied field values ($\bar{B}, B_i \in \mathbb{R}$), by linearly adding κ_0 to C_N. The para/diamagnetic contribution can be simply estimated from a linear regression of the high-field susceptibility. However, as the numerical gradient is subjected to high-frequency noise, estimating κ_0 from the magnetic hysteresis' high-field irreversible segment is less susceptible to the influence of noise. If we remove κ_0 to work directly with the ferromagnetic contribution, a forward model is then simply given as:

$$\bar{\kappa_c} = \sum_{i \geq 0}^{N} C_N \quad (5)$$

Eq. 5

2.2 Inverse model

Whilst we have arbitrarily chosen to model the lower branch, it is of course assumed that the lower and upper branches are symmetrical and centered. If not, some preprocessing must be performed to achieve more coherent results. Given a 1-D array of susceptibility data ($\bar{\kappa}$) derived from the lower branch of a magnetic hysteresis curve, and a model ($\bar{\kappa_c}$) calculated with *Eq. 5*, we expect to minimize the Euclidean norm of a squared weighted error ($\|e^2\|_2$) function as:

$$\|e^2\|_2 = \sum_{i=1}^{m} \left(\frac{\bar{\kappa}_{[i]} - \bar{\kappa}_{c[i]}}{\sigma_{\bar{\kappa}}} \right)^2,$$

Eq. 6

where $\sigma_{\bar{\kappa}}$ is measurement error for $\bar{\kappa}_{[i]}$ and m is the size of the array. Since *Eq. 5* includes non-linear terms, we cannot simply minimize *Eq. 6* through a least squares fit. Finding $\bar{p}$ (a 1D array of the parameters) that minimizes the objective function requires an iterative process. For any initial guess of the parameters ($\bar{p}_{(0)}$), correction factors ($\overline{\Delta p}_0$) for the next iteration $\bar{\kappa}_{c_{(1)}} = \bar{\kappa}_c\left(\bar{\mathrm{p}}_{(0)} + \overline{\Delta \mathrm{p}}_{(0)}\right)$ are determined using the Levenberg-Marquardt method (Aster et al., 2013; Gavin, 2022), as:

$$\overline{\Delta p}_{(0)} = \left[\left(\bar{\bar{J}}^T \cdot \bar{\bar{J}}\right) + \omega_{(0)} \cdot \bar{\bar{I}}_d\right]^{-1} \cdot \bar{\bar{J}}^T \cdot \overline{\Delta \kappa}_{(0)}$$

Eq. 7

where $\bar{\bar{J}}$ is the Jacobian matrix of $\bar{\kappa}_c\left(\bar{p}_{(0)} + \overline{\Delta p}_{(0)}\right)$; $\bar{\bar{\mathrm{I}}}_d$ is an identity matrix with the same dimensions as $\left(\bar{\bar{J}}^T \cdot \bar{\bar{J}}\right)$; $\omega_{(0)}$ is a damping factor and $\overline{\Delta \kappa}_{(0)}$ is calculated as:

$$\overline{\Delta \kappa}_{(0)} = \bar{\kappa} - \bar{\kappa}_c\left(\bar{\mathrm{p}}_{(0)}\right)$$

Eq. 8

Where the first iteration begins by adjusting the parameters so that $\bar{p}_{(1)} = \bar{p}_{(0)} + \overline{\Delta p}_{(0)}$. Obtaining $\bar{\bar{J}}$ analytically might result in singular matrixes, which is a problem that can be avoided when these derivatives ($\partial \bar{\kappa}_c / \partial p_i$) are here computed by causing small disturbances (ε) to each parameter, and evaluating their effect through a numerical central difference finite approach. We define a correction criterion (ρ_i) in order to evaluate if the adjusted parameters $\bar{p}_{(i+1)}$ better explain the observed model $\bar{\kappa}$ than $\bar{p}_{(i)}$:

$$\rho_{(i+1)} = \left| \|e^2\|_{(i+1)} - \|e^2\|_{(i)} \right|$$

Eq. 9

If $\rho_{(i+1)} > \varepsilon$:

i. $\bar{\bar{J}}$ is updated using the corrected parameters $\left(\bar{p}_{(i+1)}\right)$;
ii. $\omega_{(i+1)}$ is updated as: $\left(\gamma^{\zeta}\right) \cdot \omega_{(i)}$; where $\zeta = \frac{\bar{\kappa}_{c_{(i+1)}} \cdot \bar{\kappa}_{c_{(i)}}}{\left\|\bar{\kappa}_{c_{(i+1)}}\right\| \cdot \left\|\bar{\kappa}_{c_{(i)}}\right\|}$, as in Kwak et al., (2011);
iii. The input for the next iteration is: $\bar{p}_{(i+2)} = \bar{p}_{(i+1)} + \overline{\Delta p}_{(i+1)}$

If $\rho_{(1)} < \varepsilon$:

i. $\bar{\bar{J}}$ is not updated;
ii. $\omega_{(i+1)}$ is updated as: $\gamma \cdot \omega_{(i)}$;
iii. The input for the next iteration is: $\bar{p}_{(i+2)} = \bar{p}_{(i+1)}$

In the criteria above, ω is the damping factor that will be updated by step scaling factor γ. Both of these start with the same initial value of 0.1, as in the fixed approached of Hagan and Menhaj (1994). Iterations (i) will proceed until a convergence criterion is reached:

$$\left\| \bar{\bar{J}}^T \cdot \overline{\Delta\kappa} \right\|_2 \leq \varepsilon$$

Eq. 10

If the user has previous knowledge of the coercivity components values in the sample (i.e. from other magnetic experiments), it might be useful to constrain these B_c values. When dealing with more than one component, the user might constrain one of two of the coercivities and let the other optimize (or even constraint them all, if necessary). Care in this approach is required since the model may produce biased results due to the constraints. Inverting a component with $B_c = 0$ (i.e., a superparamagnetic population) might also cause numerical issues when calculating the Jacobian matrix (such as singular matrixes), so it is useful to constrain the solutions in this case.

The separation of components can be tested statistically by a Two-Tailed F-test, considering a null hypothesis that the variance of the data and the variance of the calculated model ($\bar{\kappa}_c + \kappa_0$) can be distinguished at a 95% confidence interval.

2.3 Monte Carlo error propagation

With the considerable number of model parameters related to each ferromagnetic component it is useful to simulate a collection of disturbed solutions to evaluate the statistical confidence of the model solutions. In our approach, we use a Monte Carlo error propagation method (Aster et al., 2013). We assume that our final inverted model produces parameters $\bar{p}_{inv}$ that faithfully represent the ferromagnetic data and introduce random noise (η) drawn from a normal distribution centered in $\bar{p}_{inv}$ and a given standard deviation. The disturbed models are calculated through *Eq. 5* with a new set of disturbed parameters ($\bar{p}_r$) by adding η to $\bar{p}_{inv}$ n-times. Sequentially running the inversion procedure (Section 2.2) allows to optimize ($\bar{p}_r$). If this procedure is repeated n times, we can produce an average model of disturbed solutions ($\overline{Pa_i}$) and then compare its difference with $\bar{p}_{inv}$ by calculating an empirical covariance estimate:

$$COV\ (\bar{p}_{inv}) = \frac{\left(\overline{Pa_i}^T - \bar{p}_{inv}{}^T\right)^T \cdot \left(\overline{Pa_i}^T - \bar{p}_{inv}{}^T\right)}{q}$$

Eq. 11

Where q is the number of parameters. Finally, the 95% confidence interval of $\bar{p}_{inv}$ is computed as (Aster et al., 2013):

$$\bar{p}_{inv} \pm 1.96 \cdot diag\left(COV(\bar{p}_{inv})\right)^{\frac{1}{2}}$$

Eq. 12

2.4 Workflow

Figure 1 shows the general workflow for the *Hist-unmix* package. The first step comprises the filtering of the lower branch of the hysteresis loop. We note that numerical derivatives through finite-differences method are strongly affected by noise, in a way that even

small disturbances can cause large spikes. To reduce these effects, we apply a simple moving average ($\bar{A}_v$) filter to the lower branch hysteresis curve:

$$\bar{A}_v = \frac{1}{L} \cdot \sum_{i=n-L+1}^{n} \bar{M}_{(i)}$$

Eq. 13

where (L) is the interval used to calculate the mean. This value will depend, logically, on the choice of the user and on the size of the sample and it is applied on the input data (the lower branch hysteresis) itself. The low-pass filter of *Eq. 13* avoids possible introduction of bias sometimes associated with polynomial/gaussian filtering. The para/diamagnetic component κ_0 is sequentially estimated from a linear regression of the high-field irreversible section of the smoothed lower branch hysteresis. The gradient of the smoothed curve is normalized by its maximum value (f) and subtracted from κ_0/f to facilitate the adjustment of the curves. Sequentially, the user should choose how many ferromagnetic components (C) will be fit to the data.

The path 1 in the workflow of Figure *1* requires the estimation of a forward model, by providing the mean coercivity (B_c), the deviation (θ), the parameters α and β, and the scale factor (I). The coercivity (B_c) must be specified within the values of the applied field (B), while θ of most of the curves will vary from zero to one (mGC functions, however, allow larger values to be tested). mGC functions can yield a large range of α and β values, but we set their initial input equal to 1 (a symmetrical approach). I parameter will normalize the contribution of the different components and its first estimation is performed automatically when the user selects the number of components. Path 2 determines a straightforward inverse model where the user simple give initial guesses without adjusting a forward model first.

To avoid getting stuck in local minima, the user can create n new array of inputs ($\bar{p}_r$) that each vary randomly up to ±20% of the standard deviation (η) of the inverted parameters $\bar{p}_{inv}$. The inverted parameters ($\bar{p}_{inv}$) with the smallest residue ($\|e^2\|$) are then used to calculate the final optimized model, which is further added to κ_0 to produce a model that represents the observed data.

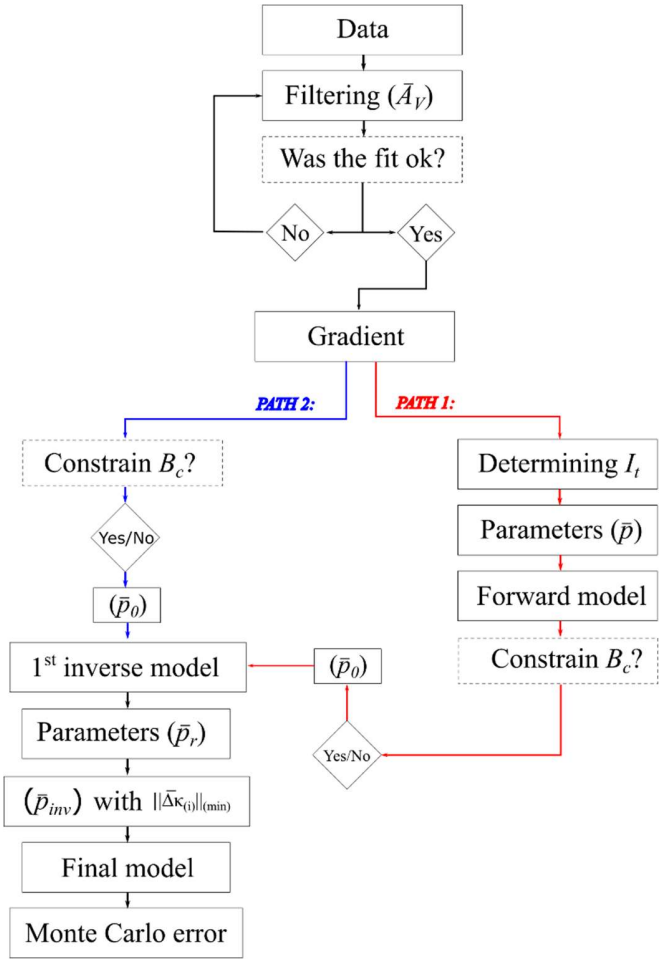

Figure 1 - Hist-unmixing workflow. $\bar{A}_v$ is the moving average filter; $\bar{p}_0$ is an array with the initial guesses for the inversion protocol; I_t is the total area of the ferromagnetic contributions; $\bar{p}_{inv}$ is an array with the optimized parameters; and $\bar{p}_r$ is an array containing a set of disturbed parameters.

A Monte Carlo error propagation is carried on to obtain the covariance of the inverted parameters and their 95% confidence interval, as well as the determination coefficient (R^2) and F-test. The creation of the set of disturbed solutions in the Monte Carlo routine follows the method described Aster et al. (2013) carried as described for $\bar{p}_r$, changing η 's standard deviation to make it following a reduced chi-squared statistic of the model produced with the inverted parameters:

$$\chi^2 = \frac{\sum_{i=1}^{N}\left(\bar{\kappa}_{[i]} - \bar{\kappa}_{c[i]}\right)^2}{N - q}, \quad \textit{Eq. 14}$$

Where q is the number of parameters.

2.5 Magnetization saturation (M_s) and saturation remanent magnetization (M_{rs})

To calculate the magnetization saturation (M_s) and saturation remanent magnetization (M_{rs}) we rely on the definite integral of the susceptibility $\bar{\kappa}$ with respect to $\bar{B}$. Since the primitive function of $\bar{\kappa}(\bar{B})$ is the magnetization $M(\bar{B})$ we can approximate M_s and M_{rs} of a given ferromagnetic component C through a numerical integration using Simpson's rule (Otto & Denier, 2005) as:

$$M_s = \int_{B_c}^{B^+} C\,(B)\,dB \approx \left(\frac{B^+ - B_c}{6}\right) \cdot \left[C_{(B^+)} + 4 \cdot \left(\frac{B^+ + B_c}{2}\right) + C_{(B_c)}\right]$$

Eq. 15

$$M_{rs} = \int_{0}^{B_c} C\,(B)\,dB \approx \left(\frac{B_c}{6}\right) \cdot \left[C_{(B_c)} + 4 \cdot \left(\frac{B_c}{2}\right) + C_{(0)}\right]$$

Eq. 16

Where $B^+$is the maximum positive applied field. Because the quality of numerical integration strongly depends on the horizontal spacing (*dB*), a one-dimensional cubic interpolation is applied to the gradient data prior the application of *Eq. 15* and *Eq. 16*.

The maximum field applied during a hysteresis procedure might not be enough to saturate a samples' magnetization. The magnetization in high-fields $\left(M_{hf}\right)$ can be expressed as (Fabian, 2006):

$$M_{hf} = M_s + (\kappa_0 \cdot B) + \left(\lambda \cdot B^{\Phi}\right),$$

Eq. 17

where λ and Φ are negative constants (called alpha and beta in Fabian's work), for which: i) Φ = -2 in homogeneously magnetized defect free-materials; ii) Φ = -1 for superparamagnetic particles; and iii) $-1 < \Phi \leq 0$ for assemblages of particles with closely spaced defects (Fabian, 2006 and references therein). Susceptibility components of *Eq. 2* are classified as Φ = -1 curves, which is not ideal for most of the natural samples. If the maximum applied field is enough to achieve an approach to saturation regime, Φ must be smaller than zero (Fabian, 2006). As *Eq. 4* results in ferromagnetic susceptibility components, we remove the induced magnetization of dia/paramagnetic contribution of *Eq. 17* $(\kappa_0 \cdot B)$ and sequentially perform its analytic derivative to obtain the high-field ferromagnetic susceptibility (κ_{hf}) as:

$$\kappa_{hf} = \frac{\partial M_{hf}}{\partial B} = \lambda \cdot \Phi \cdot B^{(\Phi-1)}$$

Eq. 18

To obtain λ and Φ, we can follow the same inversion routine described in Section 2.2 by simply changing the susceptibility terms of *Eq. 6*. For example, we calculate a synthetic model with *Eq. 18*, while considering an applied field going from 0.6 to 7T and $\Phi = -2$ and $\lambda = -2.6$ (*N=100*). These parameters are similar to those modelled in one of the curves of Fabian (2006),

where he experimentally observes that magnetization reaches saturation near 5T. By using *Eq. 18*, we observe the same as κ_{hf} tends to zero in the same field values (Figure 2a). In our inversion procedure, Φ and λ converge to the same values either for a model with the whole curve (100 points), or, limiting the field values between 0.6-1T (*N=7*, Figure 2b), showing that the lower field values within the saturation approach domain strongly might control these parameters.

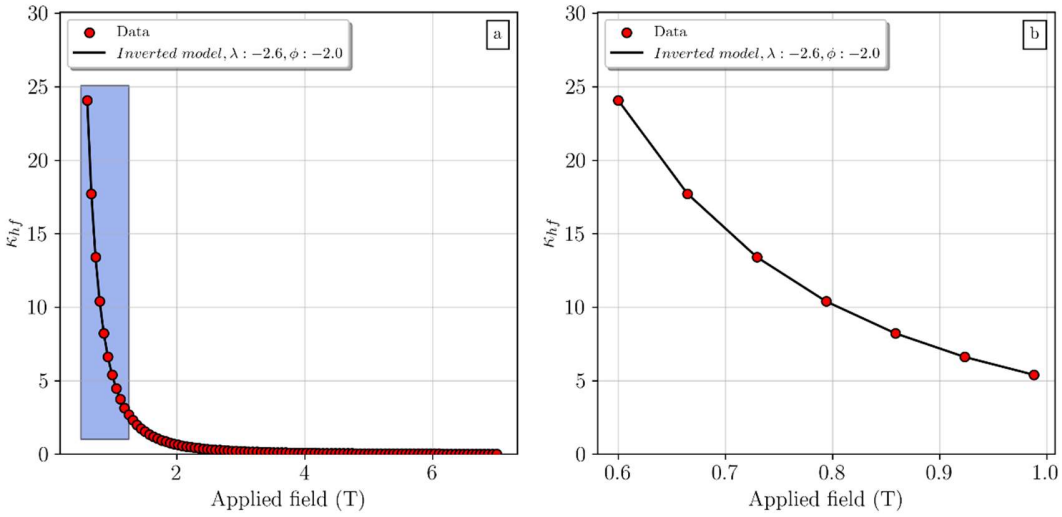

Figure 2 – Synthetic high-field susceptibility curves. a) The inversion procedure recovers mostly identical parameters for the whole synthetic curve (going from 0.6 to 7T, N=100). b) Optimization of parameters using only a small portion of the synthetic curve (bluish area in a, N=7) efficiently recovers the same parameters, which indicates that λ *and* Φ strongly controlled by lower field values within the saturation approach domain.

Nevertheless, if one decides to use this approach in the observed data, noise might decrease the effectiveness of the optimization of λ and Φ. However, as we apply this high-susceptibility validation test in the unmixed components of obtained from Eq. 6, that is not an overall issue. For a given ferromagnetic component, if $\Phi < 0$, we consider the M_s obtained from *Eq. 15* a valid saturation magnetization. If not, we can correct it using the respective inverted λ and Φ parameters.

3 Model sensitivity

We tested sensitivity of our model by creating a series of synthetic curves. Five base curves were generated (C_1 to C_5 in Figure 3a) with distinct parameters (Table 1), as well as a number of bimodal combinations, each with 1000 field values ($\bar{B}$) between -1T to 1T. Coercivity values were simulated within known ranges of typical magnetic minerals (O'Reilly, 1984). We have varied α, β, θ and I to produce curves with distinct tails and symmetry. Since these parameters represent only ferromagnetic components, we neglect the dia/paramagnetic slope (κ_0).

A random noise with a normal distribution (B_c=*0.0 Am²*, $\sigma = \pm 5 \cdot 10^{-6} Am^2$) was added to the synthetic curves, to simulate real measurements. Measurement errors might vary according to

350 the measurement routine, the sensitivity of the equipment as well as the intensity of the
351 magnetization. First, we optimized parameters of the synthetic models with one ferromagnetic
352 component following the methodological Path 1 (Figure 1), and sequentially did the same for the
353 bimodal curves as well. For the latter, we have added a small dia/paramagnetic component (κ_0).

354 For both cases, the inversion approach produced optimized parameters whose forward
355 model result in coefficients of determination ($\boldsymbol{R^2}$) greater than 0.9 (Table 2, and Figure *4*) and
356 indistinguishable variances at 95% confidence (Two-tailed F-test). Inversion of $\boldsymbol{\kappa_0}$ for the
357 unimodal curves return non-zero values, but their magnitude compared to the ferromagnetic
358 susceptibility is negligible.

359 Table 1 – Synthetic ferromagnetic components (*C*). Coercivities B_c *(T)* ranging within known
360 values for terrestrial magnetic minerals.

	$\boldsymbol{B_c}$ *(T)*	$\boldsymbol{\theta}$	$\boldsymbol{\alpha}$	$\boldsymbol{\beta}$	$\boldsymbol{I}$	**Coercivity range**
$\boldsymbol{C_1}$	$1.0 \cdot 10^{-2}$	$1.0 \cdot 10^{-1}$	$1.0 \cdot 10^{0}$	$2.2 \cdot 10^{0}$	$1.0 \cdot 10^{-1}$	Magnetite
$\boldsymbol{C_2}$	$8.0 \cdot 10^{-2}$	$1.0 \cdot 10^{-1}$	$1.0 \cdot 10^{0}$	$6.0 \cdot 10^{-1}$	$5.0 \cdot 10^{-2}$	Pyrrhotite/ Magnetite
$\boldsymbol{C_3}$	$2.0 \cdot 10^{-1}$	$7.0 \cdot 10^{-2}$	$7.0 \cdot 10^{-1}$	$2.0 \cdot 10^{-1}$	$5.0 \cdot 10^{-2}$	Pyrrhotite/Hematite
$\boldsymbol{C_4}$	$5.0 \cdot 10^{-1}$	$3.0 \cdot 10^{-1}$	$6.0 \cdot 10^{-1}$	$1.4 \cdot 10^{0}$	$1.0 \cdot 10^{-1}$	Hematite
$\boldsymbol{C_5}$	$7.0 \cdot 10^{-1}$	$2.0 \cdot 10^{-1}$	$3.0 \cdot 10^{-1}$	$9 \cdot 10^{-1}$	$1.0 \cdot 10^{-1}$	Hematite

361

362 For the bimodal models (the curves with more than one ferromagnetic component),
363 inverted curves successfully represent the synthetic data as well. The dia/paramagnetic
364 contribution for the high-field irreversible segment explain very well the displacement of the
365 base level either for a strong paramagnetic (e.g., coming from a fabric enriched in biotite) or
366 diamagnetic influences (e.g., coming from a calcium carbonate matrix).

367 To further test our model sensitivity, we examined the influence of the i) signal-noise
368 ratio, ii) sampling of the hysteresis curves, iii) the level of contribution to the total magnetic
369 susceptibility and the proximity and dispersion of components to be inverted affect the inversion.

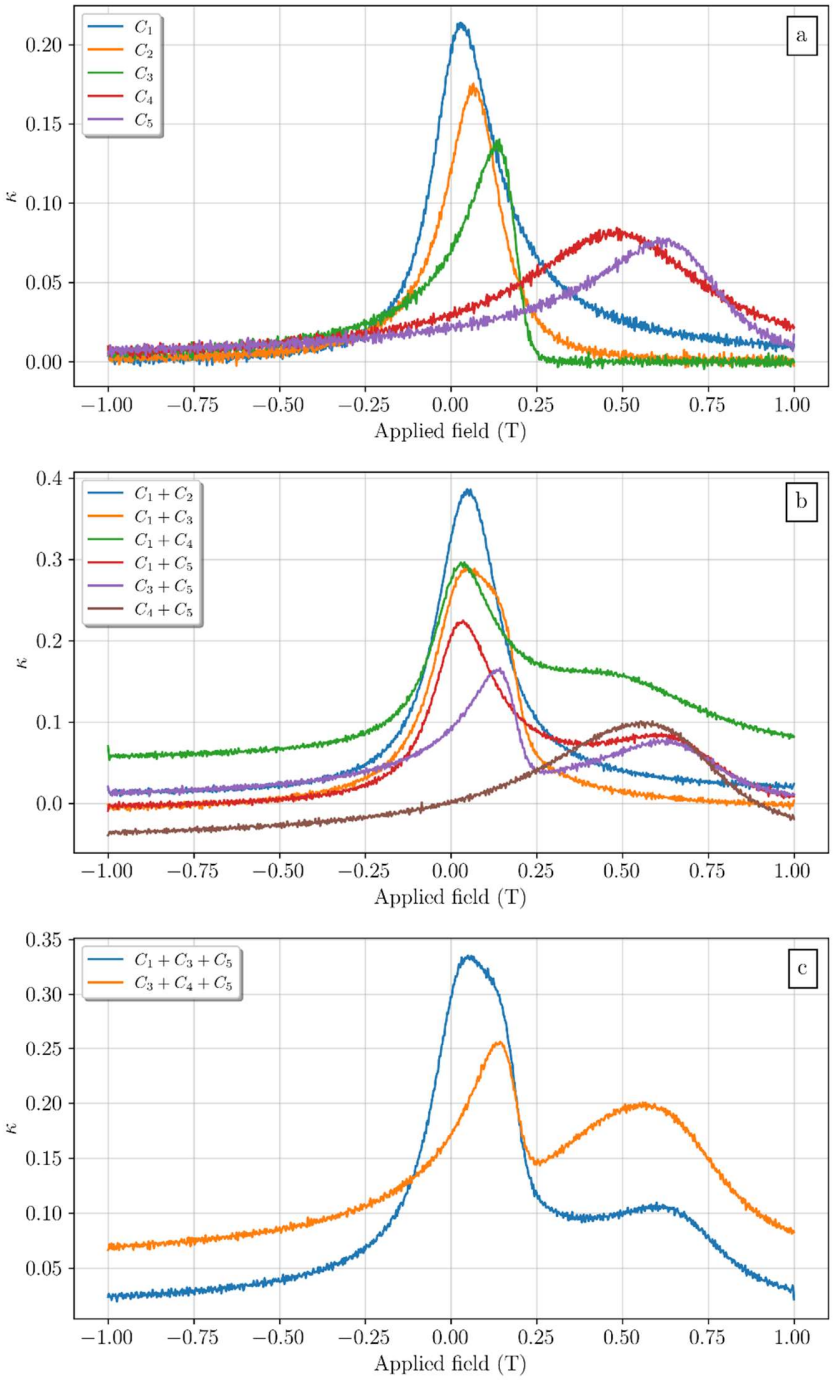

Figure 3 – Synthetic models produced using *Eq. 4*. In the case of a single ferromagnetic component (a), dia/paramagnetic slope was zeroed (check Table 1). Further examples are linear combinations of these into bimodal (c) and three-modal curves (d). A random noise was added to all the curves to represent error-measurements of real experiments.

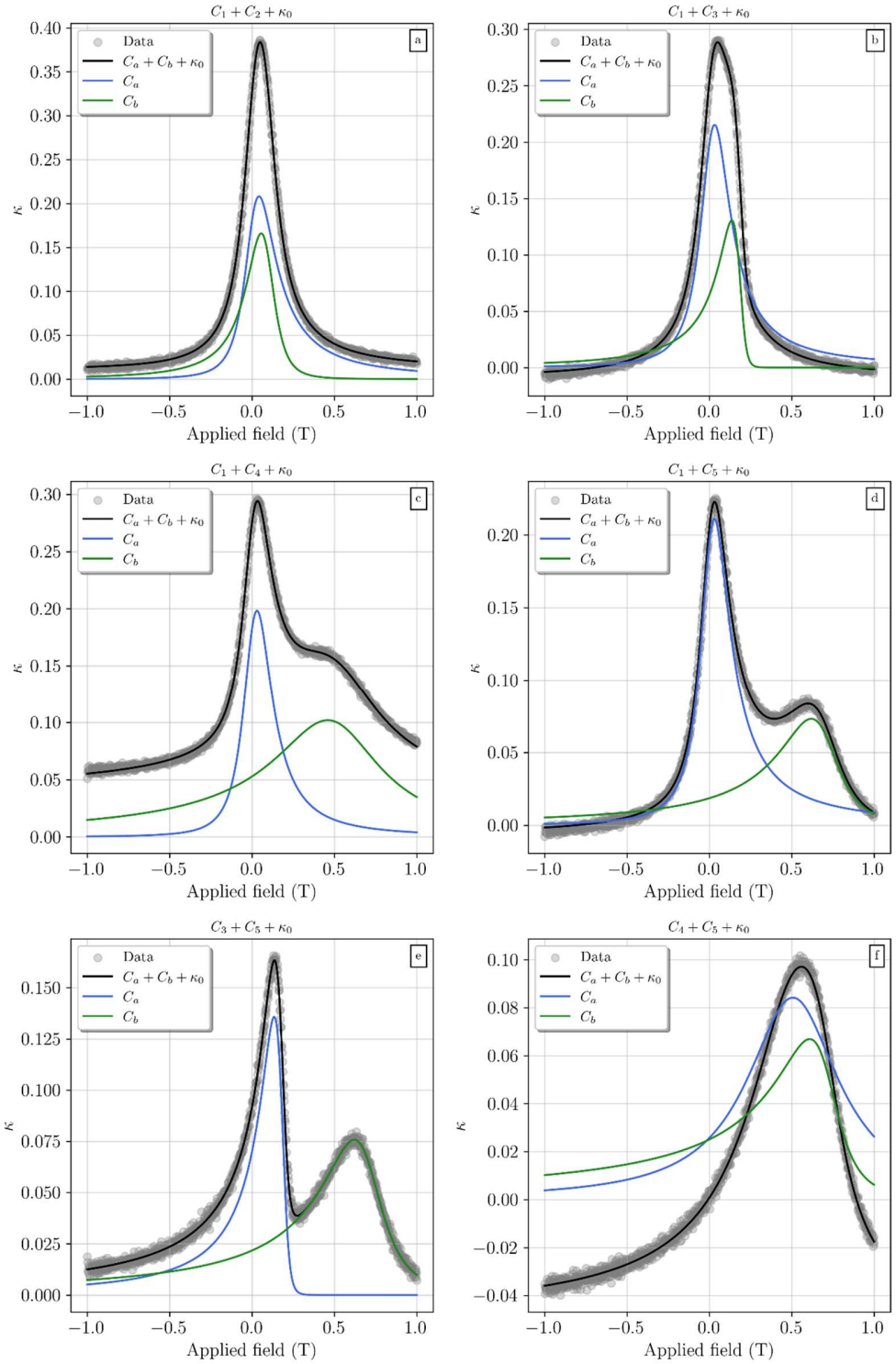

Figure 4 – Unmixing of susceptibility curves with more than one ferromagnetic component. The inversion procedure was carried by firstly adjusting a forward model to be used as input for the optimization step. C_a *and* C_b are the models calculated from the inverted parameters. Model parameters are given in Table 2.

Table 2 – Optimized parameters obtained for the unimodal and bimodal scenarios. For mixtures, the parameters of C_a and C_b components are separated by a vertical bar. $\kappa_0{}^{(s)}$ is the dia/paramagnetic susceptibility imposed to the synthetic models and κ_0 is the same parameter recovered from the inversion.

	$\kappa_0{}^{(s)}$	κ_0	$B_{c_a}(T) \mid B_{c_b}$ (T)	$\theta_a \mid \theta_b$	$\alpha_a \mid \alpha_b$	$\beta_a \mid \beta_b$	$I_a \mid I_b$	R^2	$\|e^2\|_2$
C_1	-	-	$1.02 \cdot 10^{-2}$	$9.96 \cdot 10^{-2}$	$9.5 \cdot 10^{-1}$	$2.37 \cdot 10^{0}$	$9.99 \cdot 10^{-2}$	0.998	$1.93 \cdot 10^{-4}$
C_2	-	-	$7.98 \cdot 10^{-2}$	$9.90 \cdot 10^{-2}$	$9.68 \cdot 10^{-1}$	$7.17 \cdot 10^{-1}$	$4.91 \cdot 10^{-2}$	0.998	$1.88 \cdot 10^{-4}$
C_3	-	-	$1.99 \cdot 10^{-1}$	$7.00 \cdot 10^{-2}$	$6.97 \cdot 10^{-1}$	$2.30 \cdot 10^{-1}$	$3.92 \cdot 10^{-2}$	0.997	$1.56 \cdot 10^{-4}$
C_4	-	-	$5.01 \cdot 10^{-1}$	$2.98 \cdot 10^{-1}$	$5.80 \cdot 10^{-1}$	$1.67 \cdot 10^{0}$	$7.15 \cdot 10^{-2}$	0.995	$1.49 \cdot 10^{-4}$
C_5	-	-	$6.96 \cdot 10^{-1}$	$1.96 \cdot 10^{-1}$	$2.57 \cdot 10^{-1}$	$1.04 \cdot 10^{0}$	$5.88 \cdot 10^{-2}$	0.992	$1.85 \cdot 10^{-4}$
$C_1 + C_2$	$1.00 \cdot 10^{-2}$	$1.07 \cdot 10^{-2}$	$5.94 \cdot 10^{-3} \mid 8.99 \cdot 10^{-2}$	$1.11 \cdot 10^{-1} \mid 1.12 \cdot 10^{-1}$	$1.60 \cdot 10^{0} \mid 1.08 \cdot 10^{0}$	$1.20 \cdot 10^{0} \mid 4.39 \cdot 10^{-1}$	$1.44 \cdot 10^{-1} \mid 5.54 \cdot 10^{-2}$	0.999	$2.11 \cdot 10^{-4}$
$C_1 + C_3$	$-1.00 \cdot 10^{-2}$	$-9.02 \cdot 10^{-3}$	$1.21 \cdot 10^{-2} \mid 1.97 \cdot 10^{-1}$	$1.03 \cdot 10^{-1} \mid 7.00 \cdot 10^{-2}$	$1.07 \cdot 10^{0} \mid 7.06 \cdot 10^{-1}$	$1.72 \cdot 10^{0} \mid 2.37 \cdot 10^{-1}$	$9.56 \cdot 10^{-2} \mid 3.06 \cdot 10^{-2}$	0.999	$2.09 \cdot 10^{-4}$
$C_1 + C_4$	$5.00 \cdot 10^{-2}$	$4.00 \cdot 10^{-2}$	$7.30 \cdot 10^{-3} \mid 5.05 \cdot 10^{-1}$	$1.13 \cdot 10^{-1} \mid 3.75 \cdot 10^{-1}$	$1.76 \cdot 10^{0} \mid 4.43 \cdot 10^{-1}$	$7.29 \cdot 10^{-1} \mid 1.83 \cdot 10^{0}$	$1.13 \cdot 10^{-1} \mid 1.18 \cdot 10^{-1}$	0.998	$2.20 \cdot 10^{-4}$
$C_1 + C_5$	$-1.00 \cdot 10^{-2}$	$-8.00 \cdot 10^{-3}$	$8.95 \cdot 10^{-3} \mid 7.18 \cdot 10^{-1}$	$1.03 \cdot 10^{-1} \mid 2.23 \cdot 10^{-1}$	$1.11 \cdot 10^{0} \mid 6.61 \cdot 10^{-1}$	$1.76 \cdot 10^{0} \mid 4.89 \cdot 10^{-1}$	$9.97 \cdot 10^{-2} \mid 4.88 \cdot 10^{-2}$	0.998	$1.79 \cdot 10^{-4}$
$C_3 + C_5$	-	$1.00 \cdot 10^{-5}$	$1.99 \cdot 10^{-1} \mid 6.66 \cdot 10^{-1}$	$6.98 \cdot 10^{-2} \mid 1.98 \cdot 10^{-1}$	$7.02 \cdot 10^{-1} \mid 1.98 \cdot 10^{-1}$	$2.29 \cdot 10^{-1} \mid 9.62 \cdot 10^{-1}$	$3.88 \cdot 10^{-2} \mid 5.76 \cdot 10^{-2}$	0.997	$1.69 \cdot 10^{-4}$
$C_4 + C_5$	$-5.00 \cdot 10^{-2}$	$-4.94 \cdot 10^{-2}$	$4.87 \cdot 10^{-1} \mid 7.24 \cdot 10^{-1}$	$3.46 \cdot 10^{-1} \mid 2.12 \cdot 10^{-1}$	$1.08 \cdot 10^{0} \mid 2.54 \cdot 10^{-1}$	$1.04 \cdot 10^{0} \mid 6.02 \cdot 10^{-1}$	$8.72 \cdot 10^{-2} \mid 7.65 \cdot 10^{-2}$	0.998	$1.75 \cdot 10^{-4}$

Since the data used to fit the mGC functions are the gradient of the magnetization, small perturbations might strongly affect the dispersion data. In order to test the sensitivity of the models to the proximity of different magnetic components, we can use the $C_1 + C_3$ case (Table 2), where the two components are so close that susceptibility appears as a single peak.

In this case, even curves with a high signal/noise ratio (≈0.95) can lead to a high dispersion (compare η-values in A and B scenarios, Figure 5a). However, a moving average filter seems to be very effective to remove random noise, in a way that simply choosing the *L-value* of five (*L=5*, *Eq. 13*) resulted in a good fit, with R^2*>0.9,* although the error of the less noisy data is smaller. We used the same $C_1 + C_3$ case to investigate if the two components would still be detected by reducing the sample size from 1000 points to 500 points and then to 200 points (Figure 5b). The errors increase as the number of points decrease, even though the inversion procedure satisfactorily recovered the parameters in all cases, with $R^2 > 0.9$ in all cases (Figure 5a,b).

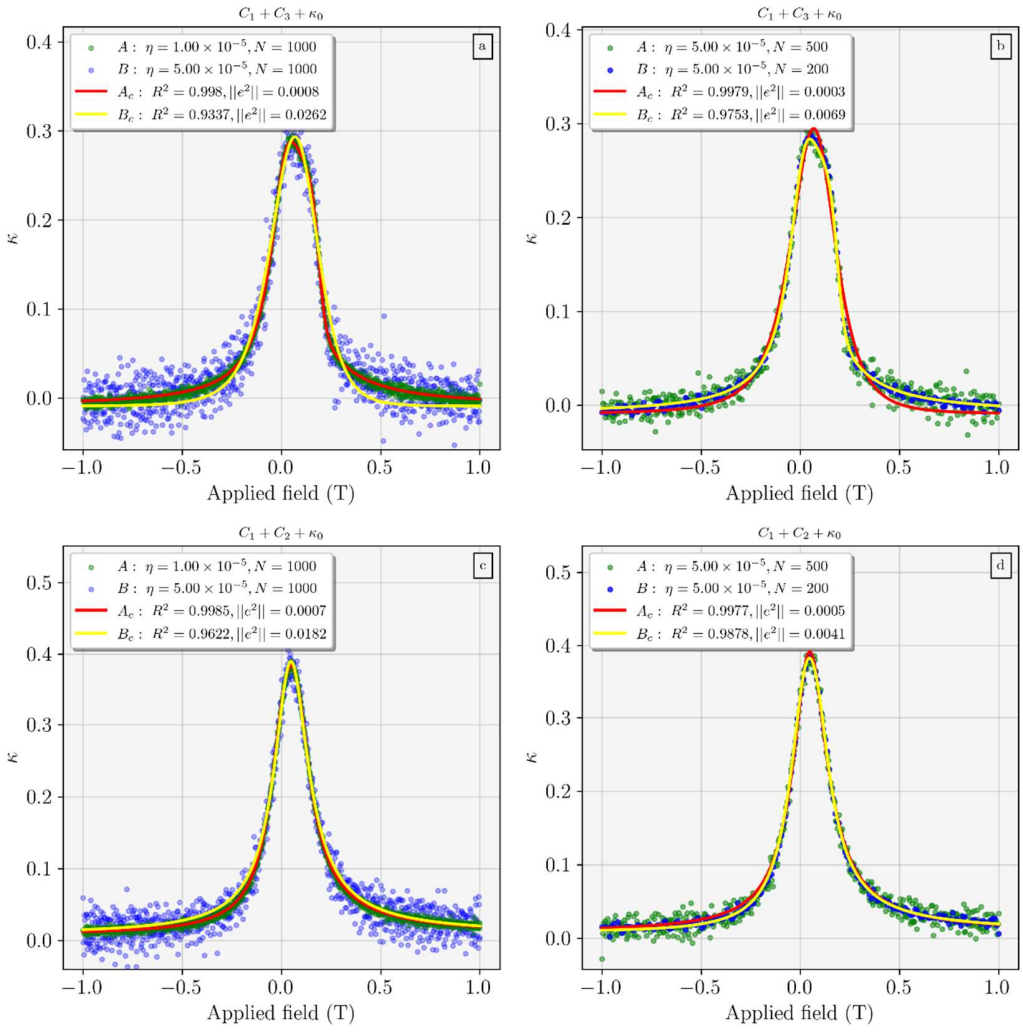

Figure 5 - Sensitivity tests in synthetic models. (a) Varying the contribution of the random noise and (b) the size of the sample for the $C_1 + C_3$ case (when parameters of the mGC curve are

considerably different). In scenarios *A* and *B*, the noise scale (η) or the number of samples (*N*) is varied. A_c and B_c are the resulted models for each of these. For the $C_1 + C_2$ case, the same tests are performed (c and d), where constraining the coercivity of one of the components using *a priori* information will produce very similar models to the observed data.

For the $C_1 + C_3$ case, the parameters are very distinct. However, in mixing cases like $C_1 + C_2$ (Figure 5c, d) where there are overlapping of distributions similar parameters, the ambiguity of the model would allow other solutions with similar residuals. This is a recurrent problem that arises with basis function' solutions to the unmixing problem, and that also affects generalized gaussian approaches to IRM unmixing (Egli, 2003; Maxbauer et al., 2016). In our case, constraining the coercivity of the C_2 component allowed us to obtain good estimates of the two distributions with little residuals in the sensitivity test for noise similar to that obtain for the $C_1 + C_3$ mixture. Without *a priori* information that would allow constraining the coercivity value of a particular component would just be justified if is available. Otherwise, we would recommend the simplest model to explain the observed data. Similar issues as seen as we increase the number of components in the sample, exemplified by the two cases shown in Figure *3*c. In the case of the $C_1 + C_3 + C_5$ mixture, the resulting morphology of the curve allows a clear distinction of at least three components and inversion of $C_a, C_b \; and \; C_c$ curves result in a fitting with indistinguishable parameters of those that form the original data (Figure 6a).

For the $C_3 + C_4 + C_5$ case, the mixing of the most coercive fractions produces a broad peak. Since the position of the component of smaller coercivity is more evident, one could adjust two other components to explain the rest of the spectrum (Figure 6b) with an almost negligible residual. However, it is also possible to explain the same curve with a composition of only two components (Figure 6c) with similar quality of fit. Still in this case, increasing the number of components to three (considering C_a component fixed) will limit the coercivity of the other two components to a single minimum region (Figure 6b'). However, the objective function of the $C_3 + C_4 + C_5$ case with only two components (fixing the other parameters) shows that local minima might be present (Figure 6c'). Still, our procedure to calculate a $\bar{p}_r$ vector (revisit section 2.4) allowed us to avoid the local minimum in Figure 6c'). Nevertheless, assuming that more than two components explain the susceptibility data should only be considered in cases where *a priori* information is available, or if the shape of the curve clearly indicates their respective contributions.

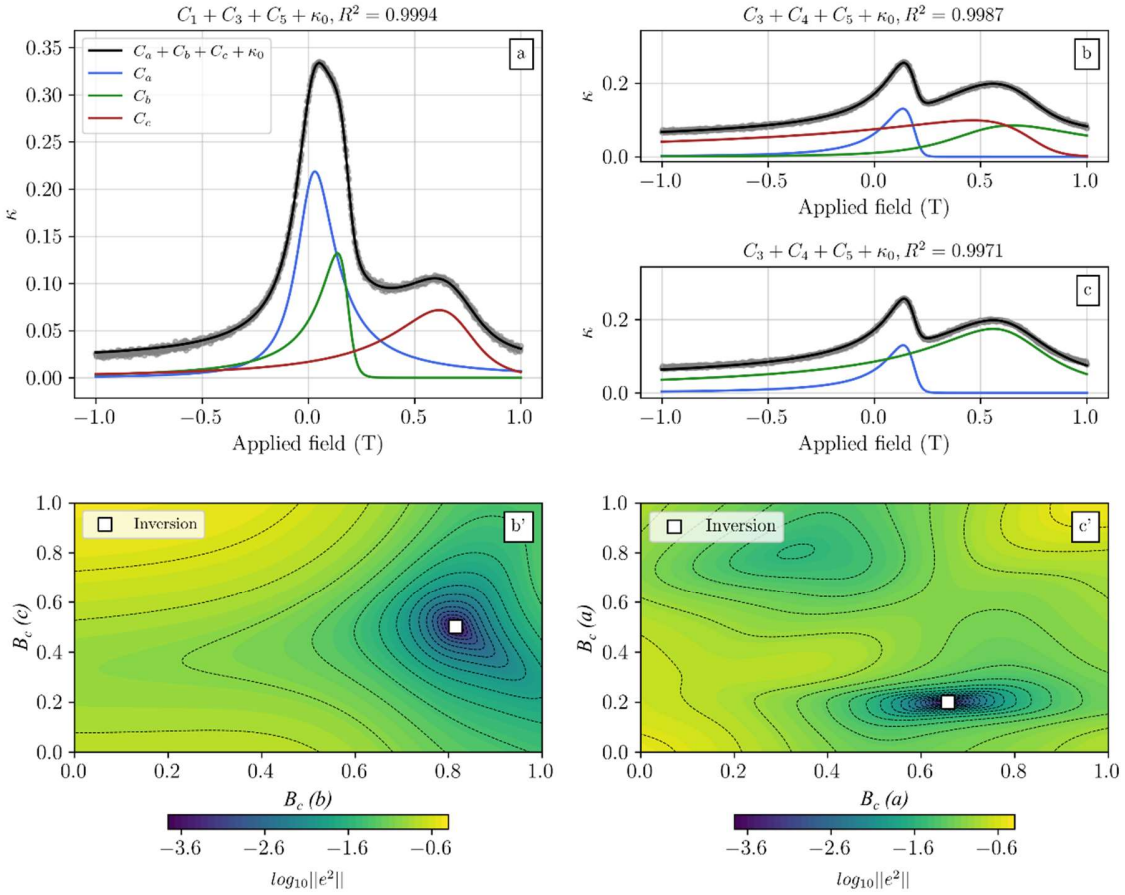

Figure 6 – Three-component case inversion. a) the shape of the curve indicates the presence of at least three different components, which are easily inverted through Hist-unmix package. However, for the $C_3 + C_4 + C_5$ case, three (b) or two components (c) explain can explain the data. When plotting the *log* of the objective function for variable coercivities (B_{c_c} and B_{c_b}) while fixing μ_a and the other parameters (b') shows that a single minimum can explain the data. However, by assuming a two-component case for the $C_3 + C_4 + C_5$ curve and fixing all of the other parameters with exception of the coercivities (B_{c_a} and B_{c_b}), a local minimum arises. Nevertheless, our inversion procedure reaches the global minimum in both explored cases (white square).

Finally, we will evaluate the presence of superparamagnetic particles (SP) as one of the susceptibility components. As shown by Tauxe et al. (1996), potbellied and wasp-waisted magnetic hysteresis can be generated by mixing SP with stable SD particles. To examine this, we construct a ferromagnetic mixture as the sum of an assemblage of superparamagnetic particles ($B_c = 0\ T$) with a higher coercive fraction (i.e. SD magnetite, $B_c = 0.07\ T$), and another one with a ferromagnetic low coercive fraction ($i.e., MD$ magnetite, $B_c = 0.002\ T$), all with the same dispersion. This is the most extreme scenario for, since reproducing the same parameters only varying the coercivity will make the identification of a superparamagnetic fraction a hard task because the difference in coercivity is very small.

We can evaluate the distortion of the curves with two components by varying their contributions (by adjusting I) to the final synthetic curve. As the contribution of C_{SD} increases, the SP particles becomes less significant (Figure 7a) but one can still identify that such curve is not perfectly matching the purely SP component. The same is valid if C_{SP} is mixed with the less coercive component in the same proportions (Figure 7c), but in this case it becomes intrinsically hard to distinguish the SP component even if its contribution is equal to the C_{MD}.

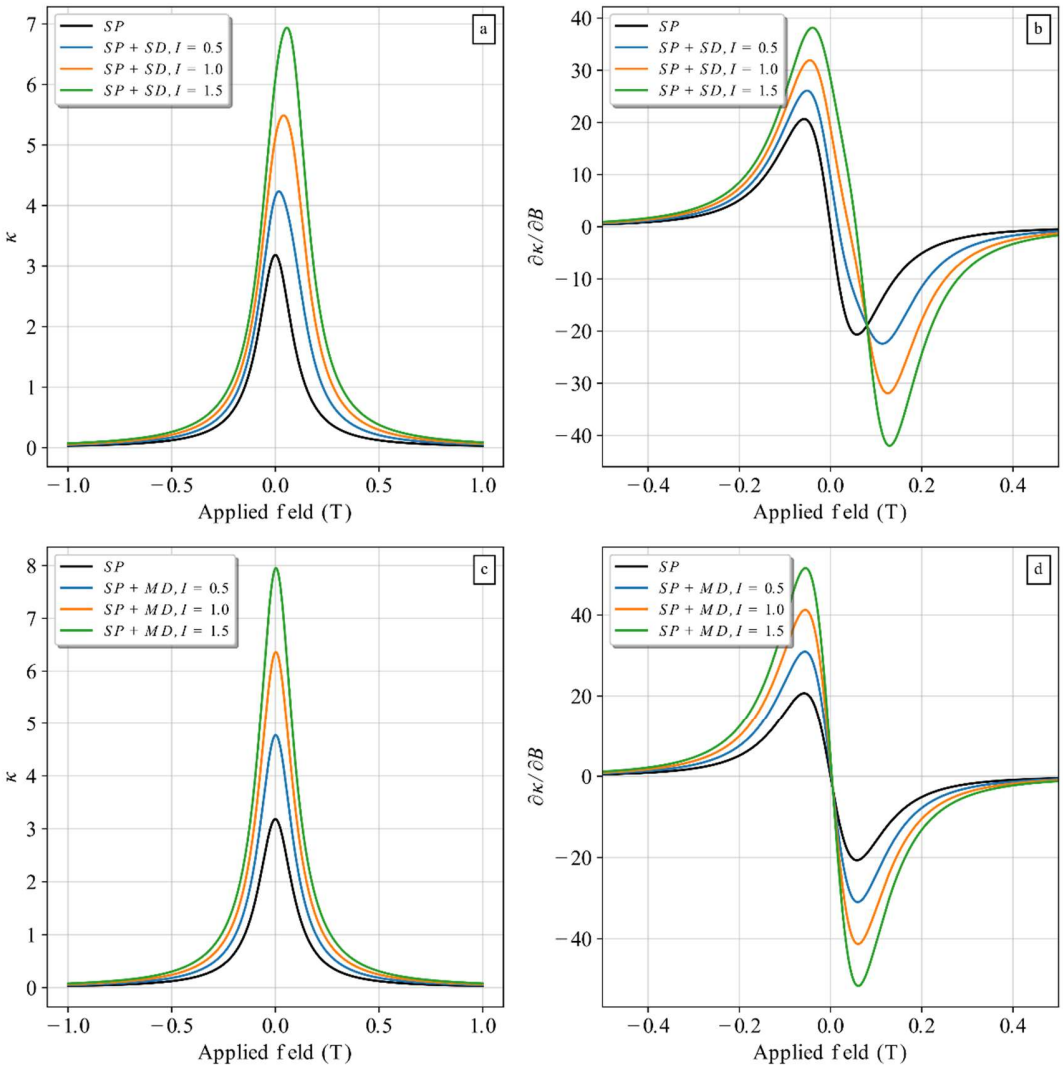

Figure 7 – Testing the sensitivity of the model for mixtures of superparamagnetic fractions with more coercive populations. When simulating the same properties of SP fraction as those of SD and MD fraction (only varying B_c), it becomes difficult to distinguish the SP contribution for both cases. Constraining the coercivity of one of the components to zero allow the user to test if (mathematically) a SP population can explain part of the observed curve. For the SP populations, I is fixed at 1.

When we calculate the second derivative of the lower branch of these hysteresis curves, this observation becomes even clearer. For C_{SP+} C_{SD} mixing cases, the derivative curve will not cross at zero field (Figure 7b), indicating the presence of a magnetic population with larger coercivity. Meanwhile, because C_{SP} and C_{MD} components coercivities are very close, the second derivative of their mixture crosses zero much closer to the origin (Figure 7d). Nevertheless, if there is *a priori* information of the presence of SP particles then constraining the one component to have zero coercivity enhances the correct identification of the remaining fractions

4 A case study on Neoproterozoic remagnetized carbonate rocks

4.1 The Sete Lagoas and Salitre formations and their magnetic signature

Remagnetized carbonate rocks are long known for their anomalous hysteresis ratios (Banerjee et al., 1997; Jackson & Swanson-Hysell, 2012; McCabe & Channell, 1994), the wasp-waisted hysteresis loops being usually considered as one of the fingerprints of remagnetization (Jackson & Swanson-Hysell, 2012) In Brazil, remagnetized Neoproterozoic carbonates typically exhibit such deformed hysteresis loops (D'Agrella-filho et al., 2000; Trindade et al., 2004). The São Francisco craton comprises two shallow-marine carbonate units, Sete Lagoas Formation and Salitre Formation, that occur in two different basins overlapping glacial diamictite successions, whose detrital zircons provided maximum ages of ~850 Ma (Babinski et al., 2012). The age of the carbonate units is estimated on the basis of detrital zircons (maximum ages of 670 and 557 Ma) (Paula-Santos et al., 2015; Santana et al., 2021) and the presence of the Cloudina fossil index in Sete Lagoas, which constrain the age of the unit to between 580 and 550 Ma.

Magnetic properties of Sete Lagoas and Salitre formations are very similar (D'Agrella-filho et al., 2000; Trindade et al., 2004): (i) wasp-waisted magnetic hysteresis, (ii) contradictory Lowrie-Fuller/Cisowski tests (Cisowski, 1981; Jackson, 1990), (iii) anomalously high hysteresis ratios, and (iv) tri-axial thermal demagnetization (Lowrie tests) with similarly behaved components. Although these formations belong to different basins and their sampling sites are separated by almost 600 km, they bear very similar paleomagnetic directions. Thermal demagnetization of these samples commonly yields up to three components (A, B and C) with very similar unblocking intervals (Figure 8a, e).

Each magnetic component can be correlated to a particular mineral assemblage depicted in the Lowrie test. The Lowrie test consists of the stepwise thermal demagnetization of three IRM acquisitions along three orthogonal axes: hard (1.3 T), intermediate (0.3 T) and soft (0.1 T). Samples from both Sete Lagoas and Salitre formations show a similar behavior in these diagrams (Figure 8d, h). The soft component shows a sluggish decay up to 400°C, a common behavior for multidomain magnetite. However, there is a steep decay of the soft component at 500°C, probably associated to the C-component of the thermal demagnetization which can be attributed to stable PSD/SD magnetite. Contrastingly, medium, and hard components of the Lowrie test are stable up to 250°C (Figure 8d), and rapidly decay at 320°C. This is close to the Curie temperature of monoclinic pyrrhotite. This mineral is correlated to the B-component disclosed for the Sete Lagoas and Salitre formations.

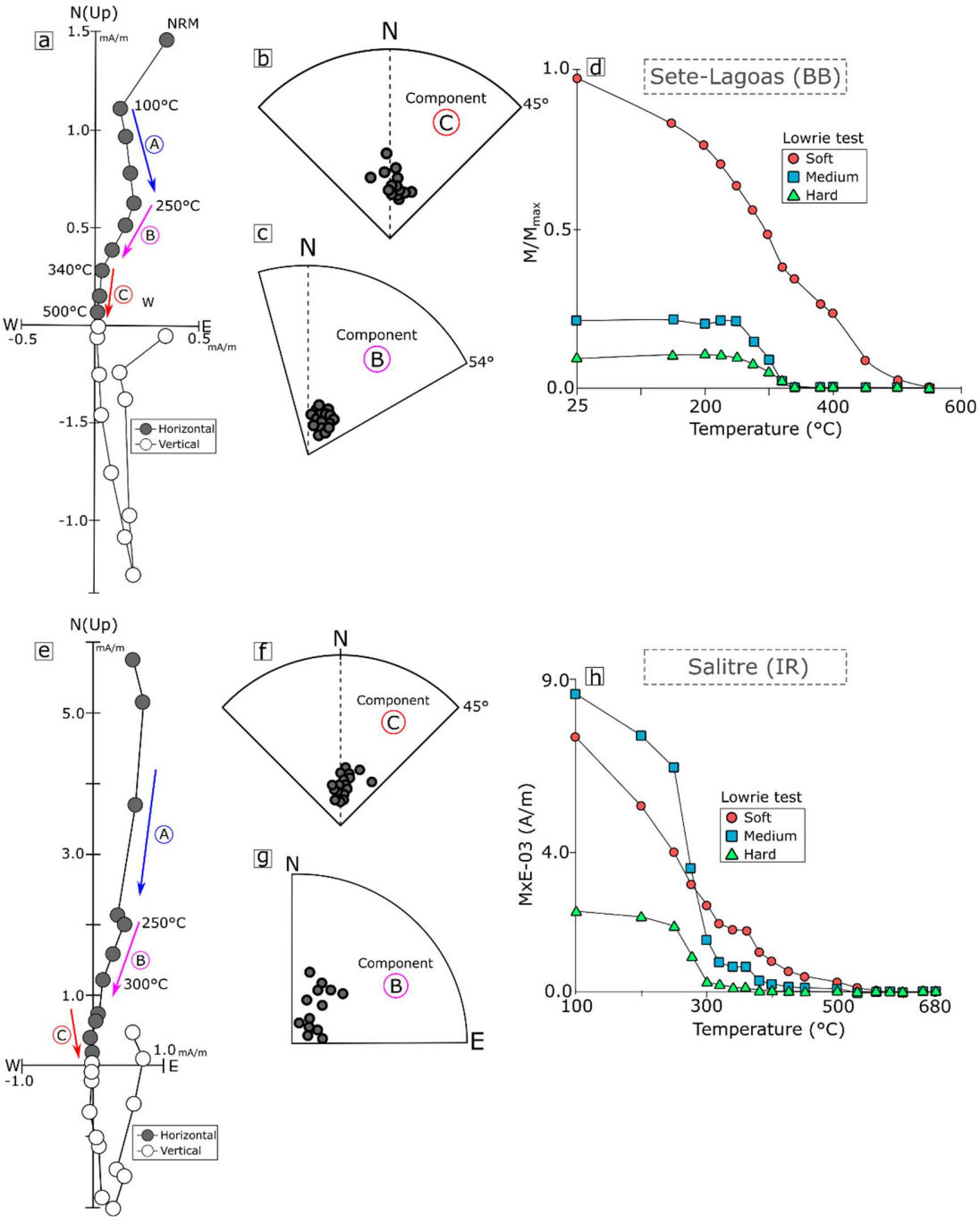

Figure 8 - Paleomagnetism and magnetic mineralogy of Sete Lagoas (BB) and Salitre (IR) formations. (a) Zijderveld diagram of a thermally demagnetized sample from the Sete Lagoas Formation, (b) the mean-site directions of C-component and (c) B-component. In (d) Lowrie-test results for a sample from the Bambuí formation. (e), (f), (g) and (h) are the equivalents for the Salitre Formation. Data acquired from D'Agrella et al (2000) and Trindade et al (2004).

512 The magnetic signature of these carbonates is interpreted, as suggested from Pb isotopic
513 data (D'Agrella-filho et al., 2000; Trindade et al., 2004), as a result of a large-scale
514 remagnetization throughout the São Francisco Craton, as caused by the percolation of orogenic
515 fluids during the final stages of the Gondwana assembling. In this way, the B and C-components
516 of both basins would be contemporary and result of craton wide chemical remagnetization. The
517 fact that these rocks present more than one stable component, likely carried by different
518 magnetic minerals with contrasting magnetic properties, makes them an interesting case study to
519 apply the Hist-unmix package. In this section, we have selected samples of each of these
520 formations (Sete Lagoas and Salitre) and performed the acquisition of magnetic hysteresis curves
521 to test the Hist-unmix package.

522 **4.2 Experimental methodology**

523 Eight samples of the Sete-Lagoas (BB) and Salitre (IR) formations (each) were separated
524 for the experimental procedure. Firstly, small fragments ($\approx$1cm³) were cut from the typical
525 cylindric samples used in paleomagnetic investigations, using a non-magnetic saw. Then, each
526 sample was bathed-in an acid solution (HCl, 10%) for about 5 seconds to get rid of any
527 superficial contamination, put into an ultrasonic bath (20 min) with ultra-pure water to neutralize
528 any remaining reaction and/or get rid of impurities incrusted in its surface. Samples were
529 consecutively dried in a silica desiccator (at 25°C) until humidity was lost. A precision balance
530 was used to measure the mass of the samples, in order to normalize the subsequent magnetic
531 measurements.

532 Magnetic hysteresis was performed with a vibrating sample magnetometer (MicroMag
533 3900 Series VSM), using a discrete sampling approach from -1T to 1T, totaling 1000 data points
534 for each sample. Processing followed the steps provided in Section 2.4 (Path 1), not constraining
535 the coercivity for any of the curves and allowing 300 models ($\bar{p}_r$) to run for each of the
536 hysteresis loops.

537 **4.3 Modelling with Hist-unmixing**
538
539 Data from both Sete Lagoas and Salitre formations have typical signatures of mixing
540 components in magnetic hysteresis. Samples from Sete Lagoas present constricted middles
541 (wasp-waisted, *Figure 9*a, b) while Salitre samples show spreading middles (potbellies, *Figure*
542 *9*c, d). It is worth to note that although these are carbonate rocks, the paramagnetic contribution
543 completely overcomes the diamagnetic response of calcite and dolomite. This paramagnetic
544 contribution (*Figure 9*e) is probably caused by the presence of terrigenous (essentially Fe-
545 bearing clay-minerals) in these rocks. To avoid any bias, the lower branches of the hysteresis
546 curves were smoothed using small L-values (*Eq. 13*, L<5). None of the samples could be simply
547 fitted by a single susceptibility component without inducing large errors. The models were
548 calculated assuming of two magnetic components (e.g., Figure *11a, b*) and resulted in $R^2 > 0.98$
549 with indistinguishable variances from a two-tailed F-test.

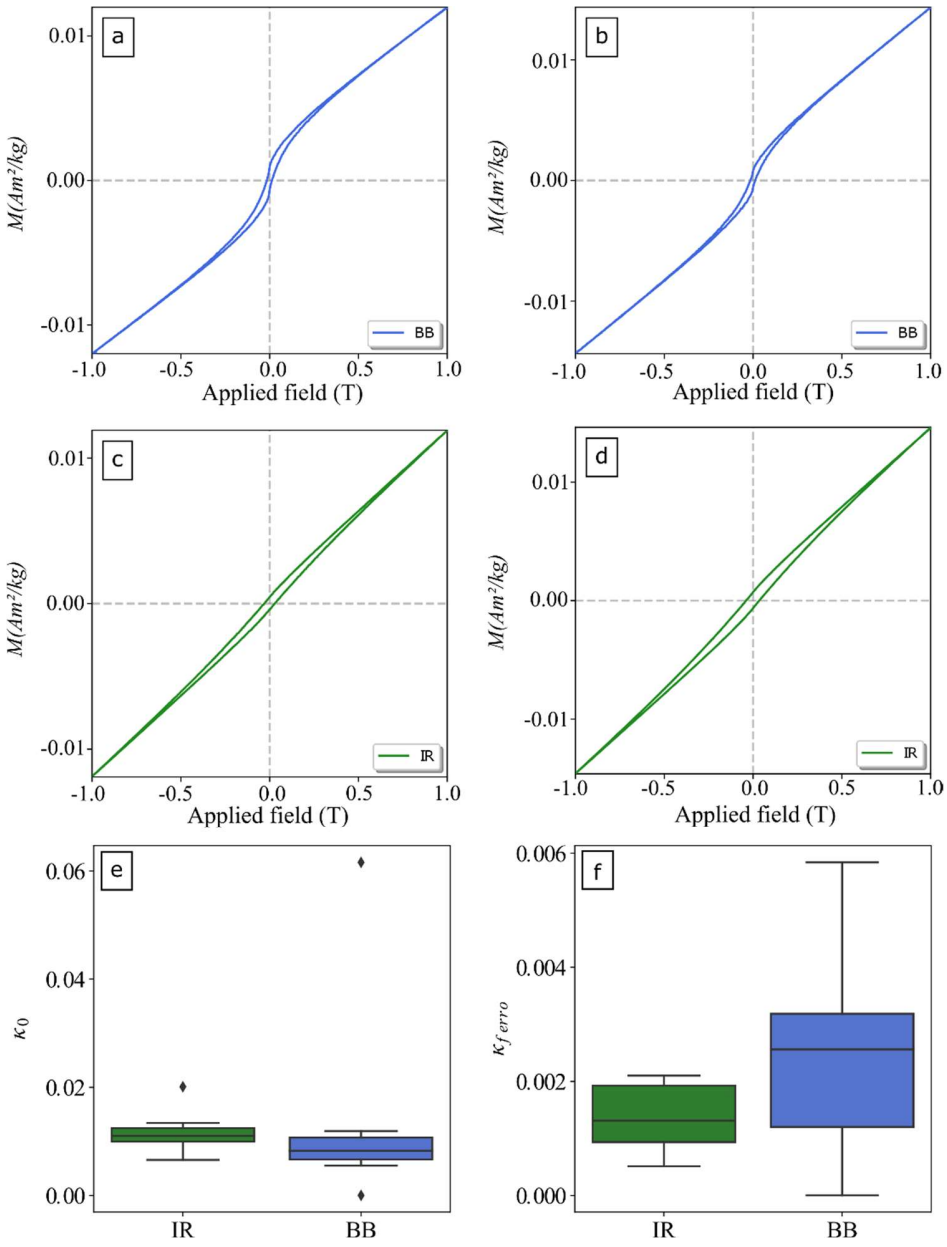

Figure 9 - Characteristic magnetic hysteresis of carbonate samples for Sete Lagoas (a and b, BB samples), and Salitre (c and d, IR samples) formations. Samples are not corrected for diamagnetic/paramagnetic contributions, since these are accounted for in our model. Boxplots (e and f) indicate the modelled contributions of paramagnetic (κ_0)and ferromagnetic (κ_{ferro}) fractions, respectively for Sete Lagoas and Salitre formations.

Boxplots distributions compiling the results of the inversions are shown in Figure *10*. Both Sete Lagoas and Salitre samples show magnetic components with very distinct coercivities (B_c-*values*). For the Sete Lagoas formation, the component with the lowest coercivity (C_a) has a median ≈ 1.7 mT, with minimum and maximum values of ≈1.0 and 11.0 mT (Figure *10*a), with an asymmetric distribution. For the component with the highest coercivity (C_b), the median is 50

mT, with maximum and lower values of 260 mT and 15 mT respectively (Figure *10*a). Saturation magnetization (M_s, Figure *10*b) is similar for both components, which implies that they contribute almost equally to the whole susceptibility spectrum. The shape of the susceptibility curves, however, are quite distinct. C_a components have a small dispersion (θ), being constricted to the region around the median, while C_b components have greater dispersion, spreading throughout a wide range of coercivities. For Salitre formation samples, the C_a components also have an asymmetric distribution, with median coercivity value of ≈ 0.6 mT and minimum and maximum values ≈ 0.098 and 11 *mT*, respectively (Figure *10*d). Bulk coercivities of C_b components are mostly higher than those of the Sete Lagoas samples. Minimum and maximum values are ≈95 and 244 *mT*, respectively and the median is 200 mT (Figure *10*d).

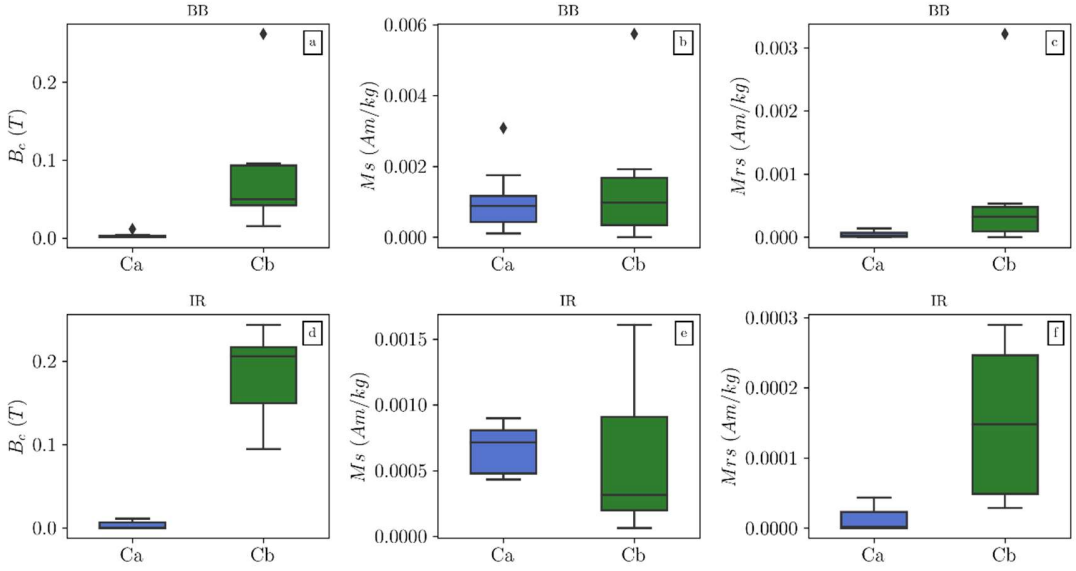

Figure 10 - Boxplots distributions of the low (Ca) and high (Cb) susceptibility components of samples from the Sete Lagoas (a to c) and Salitre (d to f) formations, obtained after modelling with Hist-unmix. Diamonds are statistical outliers.

For both Sete Lagoas and Irecê formations, coercivity boxplots of C_a are quite short and match the expected values for magnetite. We suspect that the smallest coercivity values may arise from a population of near superparamagnetic grains. Although the C_b component could be related to more than one high coercivity mineral, such as hematite or pyrrhotite, the contribution to remanence is comparable or higher than that of C_a (Figure *10*c, f). Since the remanence of hematite is much smaller than that of magnetite, it must exceed 95 wt% of the magnetic population of magnetite to influence the magnetic parameters of an assemblage formed by the hematite+magnetite mixing (Frank & Nowaczyk, 2008). Such a high proportion of hematite in these samples would contradict previously published thermal demagnetization data (Figure *8*a, *b*) as well as the Lowrie tests shown in Figure *8*d, h. this implies that the higher coercivity phase is likely to be monoclinic pyrrhotite.

Most of the modelled curves did not yield a significant asymmetry, so that a simple Lorentzian model (such as those from Vasquez and Fazzito, 2020) could have successfully explained the observed data as well. Nevertheless, some curves (e.g., Figure *11*a) might require a

589 more complex model that accounts for distinct degrees of kurtosis and skewness, which is better
590 accommodated by the modified gamma-Cauchy exponential function.

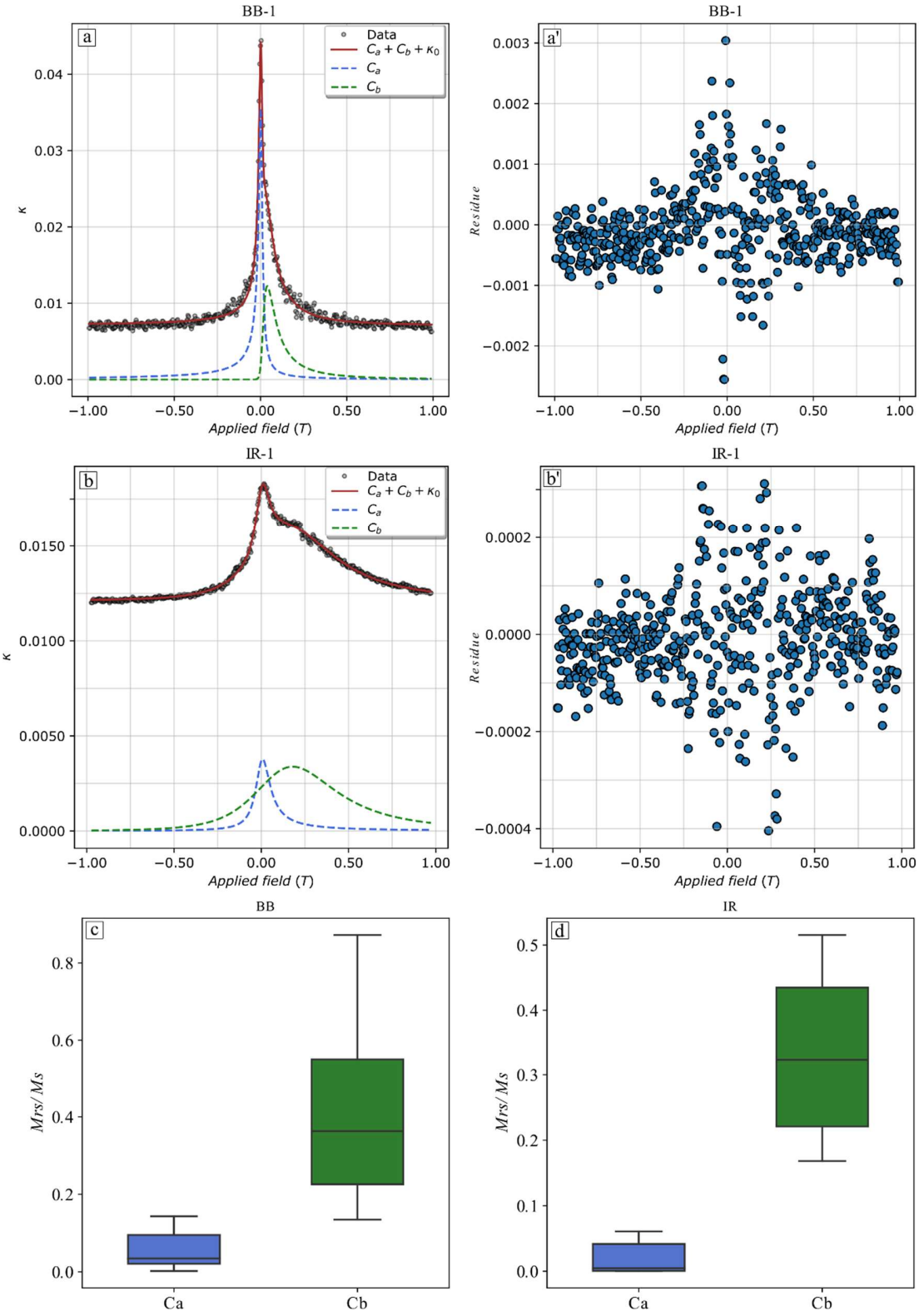

Figure 11 – Examples of the inversion procedure for samples of the Sete Lagoas (a and a') and Salitre (b and b') formations, showing the lower and higher coercive components (C_a and C_b,

respectively). The paramagnetic contribution is represented by the separation of the ferromagnetic components (blue and green lines) from the whole susceptibility spectrum. (c) and (d) are the M_{rs}/M_s ratios (calculated) for the C_a and C_b components.

Both C_a and C_b components of the two sets of samples plot mainly between the SD and MD fields of the Day plot diagram (Day et al., 1977; D. J. Dunlop, 2002). In this diagram, smaller grain sizes tend to have higher M_{rs}/M_s ratios. C_a component (whose M_{rs}/M_s ratios are below 0.2 and are greater than 0.02) would be represented by larger grain sizes within the PSD threshold (the yet poorly understood multivortex state) or in within the mixing trends of MD+SP particles. The M_{rs}/M_s ratios of both components vary widely because of the authigenic origin of these particles. The compositional heterogeneities in the sedimentary column affects how much iron is available within a region. This leads to different sizes of particles in different locations (depending on how fast the chemical reactions occur and the thermodynamic favorability of their growth). If C_a component is a mixture between MD+SP particles of magnetite, the presence of coarser grains (MD) is supported by the small B_c values modelled for this component, which could explain the viscous component observed in the thermal demagnetization procedures (Component A, Figure *8*a, e).

C_b component (whose M_{rs}/M_s ratios are usually greater than 0.2) would correspond to either a mixture of SP+SD particles (following the SP+SD mixing trends) or could represent a population with a mixture between equidimensional SD particles + the thinnest particles in the PSD range. Therefore, the assemblage of particles forming the C_b component are probablythe most stable carries of remanence in these carbonate rocks. Some of the ratios of C_b component tresspass the 0.5 threshold of the Dayplot diagram. In non-equidimensional grains, where the magnetization is strongly controlled by uniaxial shape anisotropy, the M_{rs}/M_s ratio for an SD particle is 0.5. But in equidimensional particles, whose magnetization is controlled by magnetocrystalline anisotropy, the M_{rs}/M_s ratio can be significantly higher (e.g., 0.866 for magnetite - Dunlop, 2002).

Remagnetized carbonate rocks usually plot along the power law trend controlled by cubic magnetocrystalline anisotropy (Jackson & Swanson-Hysell, 2012). This behavior was originally attributed to an authigenic origin for magnetite resulting in equidimensional grains lacking significant shape anisotropy (Jackson, 1990). Jackson and Swanson-Hysell (2012) have shown, however, that such interpretation is not necessarily correct. They attribute M_{rs}/M_s ratios above the 0.5 threshold in previous work of Jackson (1990) as experimental bias caused by a maximum applied field not being enough to saturate the samples (which was around 0.3 T in most of the samples) and experimentally show that shape anisotropy was actually dominant in their remagnetized carbonate samples. Furthermore, these power law trends (when bellow the 0.5 threshold) might as well match with SD+SP mixture trends (as compared with Dunlop, 2002). However, in our work, we apply a maximum field of 1T and provide a high-field saturation test following Fabian (2006) to attest that both C_a and C_b components are saturated in our maximum applied field. Euhedral and spheroidal iron oxides have been detected in our samples through previous SEM-EDS studies (D'Agrella-filho et al., 2000), so we suggest that a considerable amount of these could indeed contribute to the anomalous M_{rs}/M_s ratios calculated for the C_b component.

637 The magnetic data suggest that the major cause in the distorted hysteresis loops in the
638 Sete Lagoas and Salitre formations are populations of magnetic minerals with distinct
639 coercivities. These different populations can be different magnetic minerals, for example
640 magnetite and pyrrhotite, or different grain sizes of magnetite. For instance, high frequency
641 dependent susceptibilities reported by previous works suggest that superparamagnetic particles
642 likely contribute to the magnetic mineralogy of these rocks. But as argued in section 3.0, the
643 hysteresis loops are disturbed only when the fraction of superparamagnetic particles is
644 significantly high, which might be the case for C_a components with the lowest coercivity values.

645 An important clue to understanding the remagnetization in these carbonate rocks comes
646 from further information obtained from the modeling with Hist-unmixing: the significant
647 paramagnetic component apparent in samples from both the Sete-Lagoas and Salitre formations,
648 which surpass the ferromagnetic contribution. This paramagnetic contribution is likely due to a
649 high content of clay-minerals in these rocks (Callaway & McAtee, 1985; Potter et al., 2004).
650 Clay-transformations (smectite-to-illite) are known to release Fe-ions in the medium, which
651 might allow the growth of authigenic ferromagnetic phases (Katz et al., 1998; Tohver et al.,
652 2008) responsible for chemical remagnetization. Therefore, investigating the origin of this large
653 paramagnetic response might help to better constrain the geological processes responsible for the
654 large scale remagnetization in these two basins of the São Francisco Craton.

655
656

657 **5 Conclusions**

658 We have presented a python-based open-source code to perform a parametric unmixing
659 of magnetization curves, in order to separate susceptibility components of distorted hysteresis
660 curves. Our phenomenological model is based on a modified gamma-Cauchy exponential
661 function, whose advantage lies in their capacity to explain variable morphologies, from
662 symmetrical, right or left skewed curves, and covering a wide range of kurtosis.

663 *The Hist-unmix* is an easy to use python application includes a pre-processing interface,
664 where the lower branch hysteresis data is filtered through a moving average. Forward models
665 allow the user to adjust up to three ferromagnetic components and to estimate dia/paramagnetic
666 contributions. The parameters controlling each component can be subsequently optimized
667 through a Levenberg-Marquardt method. The mean coercivity of ferromagnetic components can
668 be fixed using *a priori* information, in order to constrain the solutions. Uncertainty of each
669 optimized parameter is estimated for the final inverse model using a Monte Carlo error
670 propagation (following the reduced chi-squared statistic of the inversion procedure) and its
671 variance is compared to the observed data in order to verify if they are distinguishable at 95%
672 confidence level (Two-tailed F-test). We also implement a test to verify (and correct, if
673 necessary) the magnetization saturation values of each component, by modifying the high-field
674 saturation approach of Fabian (2006).

675 *Hist-unmix* was applied to separate susceptibility components from wasp-waisted and
676 potbellied curves from real data from Neoproterozoic remagnetized carbonate rocks. The
677 inversion results clearly distinguished two ferromagnetic components: a less coercive (C_a) and a
678 more coercive (C_b) one. Together with the results of Lowrie tests, we attribute these components,

679 respectively to magnetite and monoclinic pyrrhotite, with different grain sizes. Our unmixing
680 results contribute to the understanding of the natural remanence bearing of these rocks. The
681 inversion also shows an important paramagnetic influence that completely overcomes the
682 diamagnetic carbonate matrix and even the ferromagnetic components. The latter possibly offers
683 a new hint that the large-scale magnetization event in the São Francisco Craton may have
684 involved clay-transformations as sources of iron to authigenic minerals.

685 **Acknowledgments**

686 The experimental procedures in this paper were performed at USPMag lab at Instituto de
687 Astronomia, Geofísica e Ciências Atmosféricas (IAG) at Universidade de São Paulo (USP). This
688 study was funded in part by the Coordenação de Aperfeiçoamento de Pessoal de Nível Superior -
689 Brasil (CAPES) - Finance Code 001, and by grants #21/00861-2 and #16/06114-6, São Paulo
690 Research Foundation (FAPESP). W.W. would like to acknowledge support from the Natural
691 Environmental Research Council through grants NE/V001233/1 and NE/S011978/1. We would
692 like to acknowledge the valuable discussion with Dr. Ramon Egli and Dr. Karl Fabian, which
693 greatly improved this work.

694

695 **Availability Statement**

696 The Jupyter Notebook with synthetic models shown in this analysis, as well as the *Hist-*
697 *unmix* package and its functions and the experimental data of this paper can be found at
698 https://github.com/bellon-donardelli/Hist-unmix.git, hosted at GitHub and is preserved at
699 https://doi.org/10.5281/zenodo.7941088,Version 05/2023, MIT License (bellon-donardelli/Hist-
700 unmix). Guidance for package installation and examples are available on the same link.
701

702 **References**

703 Alzaatreh, A., Lee, C., Famoye, F., & Ghosh, I. (2016). The generalized Cauchy family of
704 distributions with applications. *Journal of Statistical Distributions and Applications*, *3*(1),
705 12. https://doi.org/10.1186/s40488-016-0050-3
706 Aster, R. C., Borchers, B., & Thurber, C. H. (2013). Nonlinear Regression. In *Parameter*
707 *Estimation and Inverse Problems* (pp. 217–238). Elsevier. https://doi.org/10.1016/B978-0-
708 12-385048-5.00009-4
709 Babinski, M., Pedrosa-Soares, A. C., Trindade, R. I. F., Martins, M., Noce, C. M., & Liu, D.
710 (2012). Neoproterozoic glacial deposits from the Araçuaí orogen, Brazil: Age, provenance
711 and correlations with the São Francisco craton and West Congo belt. *Gondwana Research*,
712 *21*(2–3), 451–465. https://doi.org/10.1016/j.gr.2011.04.008
713 Banerjee, S., Elmore, R. D., & Engel, M. H. (1997). Chemical remagnetization and burial
714 diagenesis: Testing the hypothesis in the Pennsylvanian Belden Formation, Colorado.
715 *Journal of Geophysical Research: Solid Earth*, *102*(B11), 24825–24842.
716 https://doi.org/10.1029/97jb01893

Bellon, U. D. B., Trindade, R. I. F., & W, W. (2023). Hist-unmin_v1.0.0 (Version 05/2023). Zenodo. https://doi.org/10.5281/zenodo.7941088

Butler, R. F. (1992). *Paleomagnetism: magnetic domains to geologic terranes*. *Paleomagnetism: magnetic domains to geologic terranes*. https://doi.org/10.5860/choice.29-5708

Callaway, W. S., & McAtee, J. L. (1985). Magnetic susceptibilities of representative smectites. *American Mineralogist*, *70*(9–10), 996–1003.

Cisowski, S. (1981). Interacting vs. non-interacting single domain behavior in natural and synthetic samples. *Physics of the Earth and Planetary Interiors*, *26*(1–2), 56–62. https://doi.org/10.1016/0031-9201(81)90097-2

D'Agrella-filho, M. S., Babinski, M., Trindade, R. I. F., Schmus, W. R. Van, & Ernesto, M. (2000). Simultaneous remagnetization and U–Pb isotope resetting in Neoproterozoic carbonates of the São Francisco Craton, Brazil. *Precambrian Research*, *99*, 179–196. https://doi.org/10.1016/S0301-9268(99)00059-5

Day, R., Fuller, M., & Schmidt. (1977). Hysteresis properties of titanomagnetites: grain-size and compositional dependence. *Physics of the Earth and Planetary Interiors*, *13*, 260–267. https://doi.org/https://doi.org/10.1016/0031-9201(77)90108-X

von Dobeneck, T. (1996). A systematic analysis of natural magnetic mineral assemblages based on modelling hysteresis loops with coercivity-related hyperbolic basis functions. *Geophysical Journal International*, *124*(3), 675–694. https://doi.org/10.1111/j.1365-246X.1996.tb05632.x

Dunlop, D. J. (2002). Theory and application of the Day plot (M rs / M s versus H cr / H c) 1. Theoretical curves and tests using titanomagnetite data. *Journal of Geophysical Research*, *107*(B3), 2056. https://doi.org/10.1029/2001JB000486

Dunlop, J., & Özdemir, O. (1997). *Rock Magnetism: Fundamentals and frontiers*. (T. and M. David Edwards (Imperial College of Science, Ed.) (1st ed.). Cambridge: Cambridge University Press.

Egli, R. (2003). Analysis of the field dependence of remanent magnetization curves. *Journal of Geophysical Research: Solid Earth*, *108*(B2), 1–25. https://doi.org/10.1029/2002jb002023

Egli, R. (2021). Magnetic Characterization of Geologic Materials with First-Order Reversal Curves. In V. Franco & B. Dodrill (Eds.), *Magnetic Measurement Techniques for Materials Characterization* (pp. 455–604). Cham: Springer International Publishing. https://doi.org/10.1007/978-3-030-70443-8_17

Fabian, K. (2006). Approach to saturation analysis of hysteresis measurements in rock magnetism and evidence for stress dominated magnetic anisotropy in young mid-ocean ridge basalt. *Physics of the Earth and Planetary Interiors*, *154*(3–4), 299–307. https://doi.org/10.1016/j.pepi.2005.06.016

Frank, U., & Nowaczyk, N. R. (2008). Mineral magnetic properties of artificial samples systematically mixed from haematite and magnetite. *Geophysical Journal International*, *175*(2), 449–461. https://doi.org/10.1111/j.1365-246X.2008.03821.x

Gavin, H. P. (2022). *The Levenberg-Marquardt algorithm for nonlinear least squares curve-fitting problems*. Durham. Retrieved from https://people.duke.edu/~hpgavin/ExperimentalSystems/lm.pdf

Hagan, M. T., & Menhaj, M. B. (1994). Training feedforward networks with the Marquardt algorithm. *IEEE Transactions on Neural Networks*, *5*(6), 989–993. https://doi.org/10.1109/72.329697

Heslop, D. (2015). Numerical strategies for magnetic mineral unmixing. *Earth-Science Reviews*,

150, 256–284. https://doi.org/10.1016/j.earscirev.2015.07.007

Jackson, M. (1990). Diagenetic sources of stable remanence in remagnetized Paleozoic cratonic carbonates: a rock magnetic study. *Journal of Geophysical Research*, *95*(B3), 2753–2761. https://doi.org/10.1029/JB095iB03p02753

Jackson, M., & Solheid, P. (2010). On the quantitative analysis and evaluation of magnetic hysteresis data. *Geochemistry, Geophysics, Geosystems*, *11*(4), n/a-n/a. https://doi.org/10.1029/2009GC002932

Jackson, M., & Swanson-Hysell, N. L. (2012). Rock magnetism of remagnetized carbonate rocks: Another look. *Geological Society Special Publication*, *371*(1), 229–251. https://doi.org/10.1144/SP371.3

Katz, B., Elmore, R. D., Cogoini, M., & Ferry, S. (1998). Widespread chemical remagnetization: Orogenic fluids or burial diagenesis of clays? *Geology*, *26*(7), 603. https://doi.org/10.1130/0091-7613(1998)026<0603:WCROFO>2.3.CO;2

Kwak, Y. T., Hwang, J. W., & Yoo, C. J. (2011). A new damping strategy of Levenberg-Marquardt algorithm for multilayer perceptrons. *Neural Network World*, *21*(4), 327–340. https://doi.org/10.14311/NNW.2011.21.020

Liu, Q., Roberts, A. P., Larrasoaña, J. C., Banerjee, S. K., Guyodo, Y., Tauxe, L., & Oldfield, F. (2012). Environmental magnetism: principles and applications, 1–50. https://doi.org/10.1029/2012RG000393.1.INTRODUCTION

Maxbauer, D. P., Feinberg, J. M., & Fox, D. L. (2016). MAX UnMix: A web application for unmixing magnetic coercivity distributions. *Computers and Geosciences*, *95*, 140–145. https://doi.org/10.1016/j.cageo.2016.07.009

McCabe, C., & Channell, J. E. T. (1994). Late Paleozoic remagnetization in limestones of the Craven Basin (northern England) and the rock magnetic fingerprint of remagnetized sedimentary carbonates. *Journal of Geophysical Research*, *99*(B3), 4603–4612. https://doi.org/10.1029/93JB02802

O'Reilly, W. (1984). *Rock and Mineral Magnetism*. *Rock and Mineral Magnetism*. Boston, MA: Springer US. https://doi.org/10.1007/978-1-4684-8468-7

Otto, S. R., & Denier, J. P. (2005). *An Introduction to Programming and Numerical Methods in MATLAB*. Berlin: Springer.

Paterson, G. A., Zhao, X., Jackson, M., & Heslop, D. (2018). Analyzing Hysteresis Data Geochemistry , Geophysics , Geosystems. *Geochemistry, Geophysics, Geosystems*, *19*, 1925–1945. https://doi.org/10.1029/2018GC007620

Paula-Santos, G. M., Babinski, M., Kuchenbecker, M., Caetano-Filho, S., Trindade, R. I., & Pedrosa-Soares, A. C. (2015). New evidence of an Ediacaran age for the Bambuí Group in southern São Francisco craton (eastern Brazil) from zircon U-Pb data and isotope chemostratigraphy. *Gondwana Research*, *28*(2), 702–720. https://doi.org/10.1016/j.gr.2014.07.012

Potter, D. K., Corbett, P. W. M., Barclay, S. A., & Haszeldine, R. S. (2004). Quantification of illite content in sedimentary rocks using magnetic susceptibility - A rapid complement or alternative to X-ray diffraction. *Journal of Sedimentary Research*, *74*(5), 730–735. https://doi.org/10.1306/021304740730

Roberts, A. P., Cui, Y., & Verosub, K. L. (1995). Wasp-waisted hysteresis loops: Mineral magnetic characteristics and discrimination of components in mixed magnetic systems. *Journal of Geophysical Research*, *100*(B9), 909–924.

Robertson, D. J., & France, D. E. (1994). Discrimination of remanence-carrying minerals in

mixtures, using isothermal remanent magnetisation acquisition curves. *Physics of the Earth and Planetary Interiors*, *82*(3–4), 223–234. https://doi.org/10.1016/0031-9201(94)90074-4

Santana, A., Chemale, F., Scherer, C., Guadagnin, F., Pereira, C., & Santos, J. O. S. (2021). Paleogeographic constraints on source area and depositional systems in the Neoproterozoic Irecê Basin, São Francisco Craton. *Journal of South American Earth Sciences*, *109*(February 2020). https://doi.org/10.1016/j.jsames.2021.103330

Stoner, E. C., & Wohlfarth, E. P. (1991). A mechanism of magnetic hysteresis in heterogeneous alloys. *IEEE Transactions on Magnetics*, *27*(4), 3475–3518. https://doi.org/10.1109/TMAG.1991.1183750

Tauxe, L. (2005). *Lectures in Paleomagnetism* (1st ed.). Retrieved from http://earthref.org/MAGIC/books/Tauxe/2005/

Tauxe, L., Mullender, T. A. T., & Pick, T. (1996). Potbellies, wasp-waists, and superparamagnetism in magnetic hysteresis. *Journal of Geophysical Research: Solid Earth*, *101*(B1), 571–583. https://doi.org/https://doi.org/10.1029/95JB03041

Thompson, R. (1986). Modelling magnetization data using SIMPLEX. *Physics of the Earth and Planetary Interiors*, *42*(1–2), 113–127. https://doi.org/10.1016/S0031-9201(86)80013-9

Tohver, E., Weil, A. B., Solum, J. G., & Hall, C. M. (2008). Direct dating of carbonate remagnetization by 40Ar/39Ar analysis of the smectite – illite transformation. *Earth and Planetary Science Letters*, *274*, 524–530. https://doi.org/10.1016/j.epsl.2008.08.002

Trindade, R. I. F., D'Agrella-Filho, M. S. D., Babinski, M., Font, E., & Brito, B. B. (2004). Paleomagnetism and geochronology of the Bebedouro cap carbonate : evidence for continental-scale Cambrian remagnetization in the São Francisco craton , Brazil. *Precambrian Research*, *128*, 83–103. https://doi.org/10.1016/j.precamres.2003.08.010

Vasquez, C. A., & Fazzito, S. Y. (2020). Simple hysteresis loop model for rock magnetic analysis. *Studia Geophysica et Geodaetica*, *64*(1), 114–129. https://doi.org/10.1007/s11200-019-1942-8